HHS Public Access

Author manuscript

Dev Cell. Author manuscript; available in PMC 2025 January 22.

Published in final edited form as:

Dev Cell. 2024 January 22; 59(2): 211–227.e5. doi:10.1016/j.devcel.2023.11.029.

YAP and TAZ couple osteoblast precursor mobilization to angiogenesis and mechanoregulation in murine bone development

Joseph M. Collins[1,2], **Annemarie Lang**[1,2], **Cristian Parisi**[3], **Yasaman Moharrer**[1,4], **Madhura P. Nijsure**[1,2], **Jong Hyun (Thomas) Kim**[1,2], **Saima Ahmed**[3], **Gregory L. Szeto**[5], **Ling Qin**[1], **Riccardo Gottardi**[6], **Nathaniel A. Dyment**[1,2], **Niamh C. Nowlan**[3,7,8], **Joel D. Boerckel**[1,2,*]

[1]Department of Bioengineering, University of Pennsylvania, Philadelphia, PA, USA.

[2]Department of Orthopaedic Surgery, Perelman School of Medicine, University of Pennsylvania, Philadelphia, PA, USA.

[3]Department of Bioengineering, Imperial College London, London, United Kingdom.

[4]Department of Mechanical Engineering, University of Pennsylvania, Philadelphia, PA, USA.

[5]Seagen, Bothell, WA, USA.

[6]Department of Pediatrics, Division of Pulmonary Medicine, The Children's Hospital of Philadelphia, Philadelphia, PA, USA.

[7]School of Mechanical and Materials Engineering, University College Dublin, Dublin, Ireland.

[8]UCD Conway Institute, University College Dublin, Dublin, Ireland.

Summary:

Fetal bone development occurs by conversion of avascular cartilage to vascularized bone at the growth plate. This requires coordinated mobilization of osteoblast precursors with blood vessels. In adult bone, vessel-adjacent osteoblast precursors are maintained by mechanical stimuli; however, the mechanisms by which these cells mobilize and respond to mechanical cues during embryonic development are unknown. Here, we show that the mechanoresponsive transcriptional regulators YAP and TAZ spatially couple osteoblast precursor mobilization to angiogenesis, regulate vascular morphogenesis to control cartilage remodeling, and mediate mechanoregulation of embryonic murine osteogenesis. Mechanistically, YAP and TAZ regulate a subset of osteoblast-lineage cells, identified by single-cell RNA sequencing as vessel-associated osteoblast precursors, which regulate transcriptional programs that direct blood vessel invasion through collagen-integrin

*Lead contact and corresponding author: boerckel@pennmedicine.upenn.edu.

Author contributions: Conceptualization: JMC, AL, CP, NN, and JDB; Analysis: JMC, AL, CP, YM, MN, JDB; Funding Acquisition, Project Administration, and Supervision: JDB; Investigation: JMC, AL, CP, YM, JHK, MN; Methodology: AL, GS, LQ, RG, ND, NCN, JDB; Resources: NCN, ND, LQ, JDB; Writing: JMC, JDB; Review and Editing: all authors.

Competing interest: The authors have no competing interests.

interactions and Cxcl12. Functionally, in 3D human cell co-culture, CXCL12 treatment rescued angiogenesis impaired by stromal cell YAP/TAZ depletion. Together, these data establish functions of the vessel-associated osteoblast precursors in bone development.

Graphical Abstract

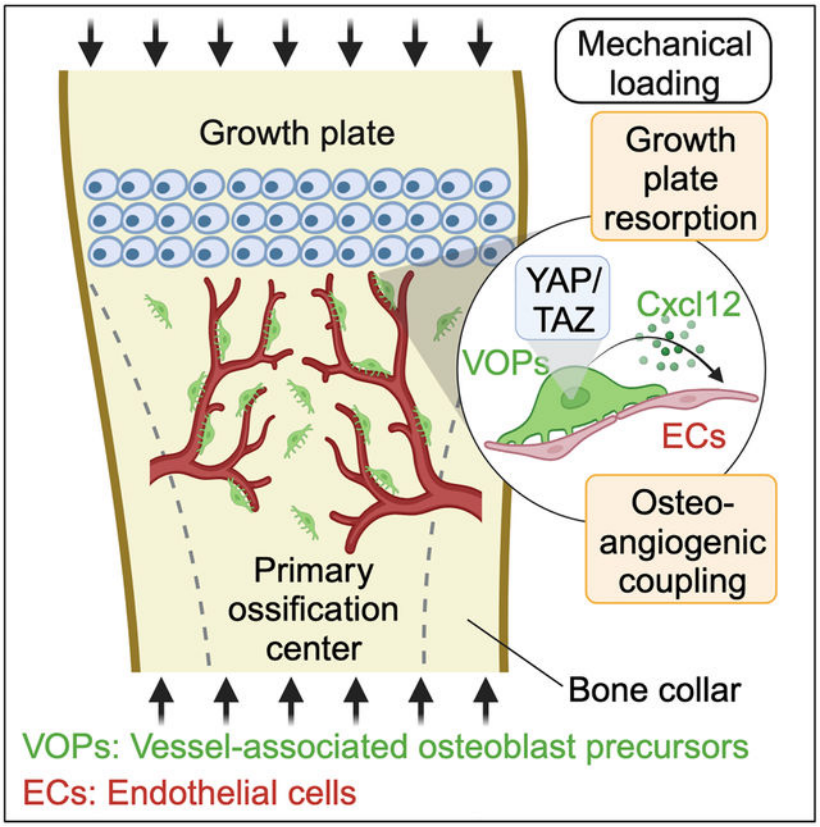

Collins et al. show that the mechanosensitive transcriptional regulators YAP and TAZ mediate the co-mobilization of osteoblast precursors with blood vessels, control growth plate remodeling through osteogenic-angiogenic crosstalk, and mediate mechanoregulation of fetal limb bone formation. Specifically, YAP and TAZ regulate a subset of vessel-associated osteoblast precursors (VOP) that regulate angiogenesis, in part through *Cxcl12* and collagen-integrin interactions.

Introduction

The appendicular skeleton forms by the conversion of avascular cartilage templates to vascularized bones, via endochondral ossification. In long bones, endochondral ossification initiates in the primary ossification center upon coordinated invasion by osteoblast precursors and blood vessels. Osterix (Osx)-expressing osteoblast precursors originate in the surrounding intramembranous bone collar and co-invade with blood vessels as pericytes[1]. Specialized blood vessels mediate cartilage matrix remodeling and localize with vessel-associated osteoblast precursors to support new bone formation[2,3]. Upon invasion, these precursors either remain vessel associated to support angiogenesis or mature into osteoblasts

for bone formation. During adult bone homeostasis, osteogenic *Lepr*$^{+}$ stromal cells in the peri-arteriolar niche respond to and are maintained by mechanical stimuli[4]; however, the mechanisms by which these cells mobilize and respond to mechanical cues during embryonic development are unknown.

During human fetal development, insufficient fetal movement (akinesia) causes skeletal defects. Fetal akinesia, caused by genetic defects in muscle development, insufficient amniotic fluid volume, or restricted movement, can lead to joint dysplasia (e.g., developmental dysplasia of the hip, arthrogryposis) and impaired fetal bone formation[5]. Normal fetal movement places high stress and strain on regions associated with akinesia-impaired morphogenesis[6], suggesting that proper skeletal development requires movement-induced mechanical cues. How these mechanical cues are transduced by skeletal cells to direct morphogenesis is poorly understood. Yes-associated protein (YAP) and transcriptional co-activator with PDZ-binding motif (TAZ) mediate mechanotransduction in osteoblast precursors *in vitro*[7], are required for persistent cell motility[8], and combinatorially regulate bone development[9,10]. Deletion of YAP and/or TAZ from Osx-expressing cells and their progeny causes perinatal lethality and severe bone fragility in mice[9]. YAP and TAZ are activated by a variety of signals, including morphogenic and mechanical cues, and regulate gene expression by transcriptional co-activation/repression of various transcription factors[11]. These data position YAP and TAZ as potential mediators of both embryonic bone morphogenesis and mechanotransduction.

Here, we show that YAP/TAZ signaling in osteoblast-lineage cells mediates bone development by regulating the co-mobilization of vessel-associated osteoblast precursors and blood vessels, in part through CXCL12 signaling. YAP/TAZ-mediated vascular morphogenesis is necessary for hypertrophic cartilage degradation and endochondral ossification. Further, YAP and TAZ are required for embryonic load-induced bone formation. Here, we show that the mechanoresponsive transcriptional regulators, YAP and TAZ, couple osteoblast precursors to vessel morphogenesis and mediate mechanical regulation during fetal bone development.

Results

YAP and TAZ mediate endochondral ossification and growth plate remodeling

We first sought to determine the roles of YAP and TAZ in embryonic bone development. In the developing bone, YAP and TAZ are expressed robustly in cells of the primary ossification center, particularly the Osterix-expressing osteoblast precursors (Fig. 1A, Fig. S1). We therefore deleted both YAP and TAZ from Osterix-expressing cells using Osx-GFP::Cre (hereafter, Osx-GFP). Osx is expressed in hypertrophic chondrocytes and osteoprogenitors and their progeny during embryonic limb development (Fig. 1A). Cre-mediated recombination effectively deleted YAP and TAZ from Osx-expressing cells in both the primary ossification center and bone collar but did not affect YAP/TAZ expression in the cartilage rudiment, early hypertrophic chondrocytes, blood vessels, or surrounding muscle (Fig. 1A). To assess early osteoblast activity, we measured alkaline phosphatase (ALP) activity, which marks osteogenesis in both the endochondral primary ossification center and intramembranous bone collar. Osx-conditional YAP/TAZ deletion significantly reduced ALP

activity in the primary ossification center (Fig. 1B,C), but did not substantially alter ALP activity or mineralization in the bone collar (Fig. 1B,C, Fig. S1). These data suggest specific roles for YAP and TAZ in endochondral ossification.

Endochondral ossification requires chondrocyte hypertrophy and remodeling. Upon hypertrophy, chondrocytes secrete a Collagen 10-rich matrix, which is degraded by endothelial cells and other cartilage-degrading cells to form the transverse cartilage septum at the chondro-osseous junction. In the primary spongiosa, the matrix is replaced by osteoblast-lineage cells. Osx-conditional YAP/TAZ deletion significantly decreased the length of the primary ossification center (Fig. 1D). Osterix-conditional YAP/TAZ deletion did not alter the location at which chondrocytes initiate collagen 10 expression upon hypertrophic initiation, but increased the length of the growth plate due to expanded hypertrophic zone length (Fig. 1E,F). Notably, YAP/TAZ deletion altered the shape of the cartilage septum, producing a conical chondro-osseous junction that extended hypertrophic cartilage into the primary ossification center (Fig. 1G,H). Together, these data indicate that YAP and TAZ mediate endochondral ossification and hypertrophic cartilage remodeling.

YAP and TAZ mediate osteoblast precursor mobilization

Endochondral ossification initiates by osteoblast precursor co-mobilization with blood vessels from the surrounding bone collar into the primary ossification center. Cells move by exerting forces on their extracellular matrix through cytoskeletal activation[8]. We mapped skeletal-lineage cells over time using triple collagen reporter mice, which express fluorophores that label chondrocytes (Col2-CFP), hypertrophic chondrocytes (Col10-RFP), and osteoblasts (Col1(3.6kb)-YFP) (Fig. 2A). Anlage chondrocytes reduced Col2-CFP expression upon maturation into Col10-RFP-expressing hypertrophic chondrocytes (Fig. 2B). Growth plate separation, indicated by distinct Col10-RFP peaks, initiated at embryonic day 15.5 (E15.5) and continued through embryonic day 17.5 (E17.5) (Fig. 2B). At E15.5, differentiated Col1(3.6kb)-YFP$^+$ osteoblasts were present in the bone collar, and appeared in the primary ossification center by E17.5. To map the cytoskeleton, we stained filamentous actin (F-actin) using Phalloidin (Fig. 2B, Fig. S2). An acute peak in F-actin intensity emerged in the middle of the primary ossification center at E15.5, marking the initiation of cellular mobilization (Fig. 2B). By E17.5, elevated F-actin staining extended as a uniform plateau throughout the primary ossification center, coincident with Col1(3.6kb)-YFP$^+$ osteoblast emergence (Fig. 2B, Fig. S2).

YAP and TAZ are activated in migrating cells by tension in the actin cytoskeleton[8]. Osx-conditional YAP/TAZ deletion had no effect on F-actin distribution at E14.5, prior to anlage invasion (Fig. 2C, S3), but prevented the emergence of the mid-diaphyseal F-actin peak at E15.5, indicating a delay in primary ossification center initiation (Fig. 2C, Fig. S3). At E17.5, Osx-conditional YAP/TAZ deletion both shortened and reduced the F-actin plateau that marks primary ossification center expansion (Fig. 2C). Previously, we found that YAP/TAZ-induced transcription cell-autonomously modulates myosin activation to maintain cytoskeletal homeostasis for persistent cell migration[8,12]. Specifically, YAP/TAZ deletion elevated F-actin polymerization and caused cytoskeletal tension-induced migratory arrest[8]. To test for YAP/TAZ regulation of the cytoskeleton in osteoblasts in vivo, we

generated $WT^{f/f}$ and YAP/TAZ cKO^{Osx} mice that additionally expressed a Col1(3.6kb)-CFP collagen reporter to mark osteoblasts. These reporter mice feature the same promoter fragment described above, but feature cyan fluorescence to avoid overlap with the Osx-GFP. YAP/TAZ deletion doubled F-actin intensity in Col1(3.6kb)$^+$ osteoblasts in the primary ossficiation center, consistent with our prior findings, but these differences were not statistically significant (Fig. 2D, E). YAP/TAZ deletion had no observable effect on F-actin levels in bone collar osteoblasts (Fig. 2D,E). Next, to directly evaluate osteoblast precursor emergence, we quantified cell density and the fraction of Osx-GFP$^+$ cells in the bone collar and primary ossification center. Osx-conditional YAP/TAZ deletion substantially reduced total cell density in the primary ossification center, but only modestly reduced total cell density in the bone collar (Fig. 2G,H). YAP/TAZ deletion significantly reduced Osx-GFP$^+$ cell fraction in the primary ossification center but did not significantly alter the fraction of Osx-GFP$^+$ cells in the bone collar (Fig. 2I–K, Fig. S4). These data suggest that YAP and TAZ mediate osteoblast precursor mobilization into the developing limb.

YAP and TAZ regulate Cxcl12 in vessel-associated osteoblast precursors

Vessel-associated osteoblast precursors (VOPs) mobilize with invading blood vessels, prior to their commitment to mature osteoblastic fate[1]. Therefore, to determine how YAP and TAZ regulate gene expression in osteoblast-lineage cells and their interaction with other cell types, we performed single-cell RNA sequencing (scRNA-seq) on embryonic forelimbs. We isolated cells from E17.5 forelimbs of $WT^{f/f}$, WT^{Osx}, and YAP/TAZ cKO^{Osx} mice (n = 3–4/genotype) for scRNA-seq using the 10X Genomics Chromium platform. To capture both osteoblast-lineage and non-osteoblast-lineage cells, we removed dead cells and lysed red blood cells, but did not sort prior to scRNA-seq. We evaluated high-quality transcriptomes from 120,292 cells (Fig. 3A). The developing embryonic limb contains a large number of cell types. We applied Louvain clustering to identify 77 clusters, categorized as 12 major cell populations by canonical marker expression[13,14]. These populations included osteoblasts, endothelial cells, and chondrocytes (Fig. 3B,C, Fig. S5–9). Each sample contained every cell population, and while there was variability between samples, there were no distinct differences by genotype (Fig. 3D,E).

We identified a single cluster, of the 77 clusters, as osteoblast-lineage cells based on gene expression patterns, including *Runx2, Alpl, Osx (Sp7), Col1a1, Spp1, Ibsp, Bglap, and Dmp1* (Fig. 3F). Osx-conditional YAP/TAZ deletion did not significantly alter the total number of osteoblasts in the developing limb (Fig. S7), but significantly altered gene expression in osteoblasts. YAP/TAZ deletion reduced expression of mineralization genes (*Spp1*, *Bglap*, *Bglap2*) and increased expression of matrix metalloproteinases (*Mmp9, Mmp14*) and adipocyte genes (*Fabp4*) (WT^{Osx} compared to YAP/TAZ cKO^{Osx}, Fig. 3G, Table S1; $WT^{f/f}$ compared to YAP/TAZ cKO^{Osx}, Fig. S7, Table S2). We did not find substantial differences in the chondrocytes (Fig. S6). One of the most-downregulated genes in osteoblasts was *Cxcl12*, which mediates mechanoregulation of bone formation, angiogenesis, and hematopoiesis[15]. Therefore, we sought to identify which of the osteoblastic cell states expressed these genes. We identified seven osteoblastic cell states by Louvain clustering, including one identified as osteoblasts that had been co-lysed with erythrocytes, based on expression of hemoglobin genes (cluster/state g; Fig. 4A, B). Similar

to the major cell types, each sample contained every osteoblast cell state, and while there was variability between samples, there were no distinct differences by genotype (Fig. 3D,E).

Only one osteoblast cell state (state 'a'), was enriched for *Cxcl12* (Fig 4B,E). Osteoblast cell state 'a' featured the transcriptional profile of vessel-associated osteoblast precursors (VOPs; Fig. 4A). Consistent with prior lineage-tracing and conditional knockout studies defining the VOPs[16,17], these cells were *Osx*$^{+}$, *Runx2*$^{+}$, *Pdgfra*$^{+}$, *Pdgfrb*$^{+}$ and *Kitl*$^{+}$. The VOPs were also enriched for *Vegfa*, *Angptl4*, and *Mmp9/13* (Fig. 4B,E, Fig. S8). Gene set-enrichment analysis showed that, compared to other osteoblast-lineage cells in composite, the VOPs were significantly enriched for gene sets associated with cytoskeletal dynamics, positive regulation of blood vessel endothelial cell migration, and cell migration (Fig. 4F). Additionally, the other osteoblastic cell states, in composite, were enriched for gene sets associated with biomineralization and osteogenesis (Fig. 4F). YAP/TAZ deletion did not significantly alter the number of VOPs (Fig. S7). We next evaluated the effects of YAP/TAZ deletion on gene expression in VOPs. Consistent with gene expression in all osteoblasts, *Cxcl12* was one of the most downregulated genes in YAP/TAZ cKO^{Osx} VOPs when compared to both WT^{Osx} (Fig. 4G, Table S3) and WT$^{f/f}$ VOPs (Fig. S7, Table S4). YAP/TAZ deletion also reduced VOP expression of the angiogenic gene, *Angptl4*, *Kitl* (which encodes SCF), and increased expression of matrix remodeling genes, *Mmp9* and *Mmp13*, but did not significantly alter *Vegfa* expression (Fig. 4H). To determine whether YAP and TAZ may directly regulate *Cxcl12* transcription, we interrogated published ChIP-seq data in which YAP or TAZ were immunoprecipitated from HUVECs and associated chromatin was isolated for DNA sequencing[18]. These data indicate that YAP and TAZ can bind directly to the CXCL12 promoter locus, with particular enrichment for TAZ (Fig. 4I). To validate YAP/TAZ regulation of *Cxcl12* expression in vivo, we performed RNAscope and observed reduced *Cxcl12* mRNA abundance in the primary ossification center adjacent to invading blood vessels (Fig. 4J). Together, these data identify general roles of YAP/TAZ signaling in fetal osteoblasts and particular roles in vessel-associated osteoblast progenitor cells through transcriptional regulation of angiogenic chemokines and growth factors.

YAP and TAZ mediate Vessel-associated osteoblast precursor (VOP)-endothelial cell crosstalk, blood vessel integrity, and hypertrophic cartilage remodeling

During limb development, VOPs co-mobilize with blood vessels and regulate angiogenesis and vascular integrity as pericytes[16,17]. Bone-resident endothelial cells represent a unique population of endothelial cells with particular structure, function, and gene expression signature. Bone- and bone marrow-resident endothelial cells have been previously identified by their expression levels of two cell-surface receptors, CD31 (*Pecam1*) and Endomucin (*Emcn*)[2,19]. Bone-resident blood vessels that are high in both CD31 and Endomucin have been labeled "Type H" and localize to the bone metaphysis where they support new bone formation[2,20]. Bone-resident blood vessels that are low in both CD31 and Endomucin have been labeled "Type L" and form the sinusoidal vasculature in the bone marrow[2]. A third population of bone-resident endothelial cells is abundant in embryonic bone, in addition to the Type H and Type L. These "Type E" vessels feature high CD31 and moderate Endomucin expression, support osteoblast-lineage cells in the developing limb, and require integrin-mediated extracellular matrix interactions for their function[19]. We identified 11

endothelial cell states in the limb by iterative clustering of the endothelial cells (Fig. 5A, Fig. S9). We identified 5 endothelial cell states (a-e) as those most likely to contain Type H or Type E bone-resident endothelial cells based on thresholds for *Emcn* and *Pecam1* expression (Fig 5B). Further, expression of the Cxcl12 receptors *Cxcr4* and *Ackr3*(Cxcr7) were predominately limited to clusters (c) and (b), respectively (Fig. 5C).

Therefore, we next asked whether Osx-conditional YAP/TAZ deletion disrupted cell-cell communication between VOPs and endothelial cell states (a) through (e). We used the cell-cell communication package CellChat, which infers interaction between ligand-receptor complexes based on subunit, agonist, and antagonist expression levels[21]. Osx-conditional YAP/TAZ deletion reduced the number of putative interactions between VOPs and endothelial cell states (a) through (e) (Fig. 5D). VOPs exhibit potential communication with endothelial cells through extracellular matrix interactions (i.e., endothelial cell integrins binding to VOP-produced extracellular matrix) and angiogenic signaling pathways (Fig. 5E). Here, a dot indicates a significant interaction, while the color reflects the communication probability (Fig. 5E). VOP-endothelial cell communication was most prominent with endothelial state (c). YAP/TAZ deletion significantly abrogated putative communication from VOPs to state (c) endothelial cells through collagen adhesion, particularly through integrin complexes α1/2-β1, Cd44, and through Cxcl12-Cxcr4 (Fig. 5E). Osx-conditional YAP/TAZ deletion moderately reduced expression of these receptors in endothelial cells, but these differences were not statistically significant (Fig. 5F). Vegfa-Vegfr1r2 communication was not disrupted for any pairing.

Together, cell-cell communication analysis revealed that the endothelial cell state whose putative communication with VOPs was most prominent and most YAP/TAZ-regulated was state (c). This endothelial cell state featured moderate *Emcn* expression and high *Pecam1* (Fig. 5C), and is consistent with the previously defined embryonic distribution, gene expression patterns, and function of embryonic “Type E” cells[19]. Like other endothelial states, state (c) did not exhibit substantial differential gene expression upon Osx-conditional YAP/TAZ deletion (Fig. S9). Further, prior studies showed that Osx-conditional Cxcl12 deletion reduced B lymphoid progenitors in the bone marrow[22]. Consistently, analysis of immune populations in our data set showed Osx-conditional YAP/TAZ deletion caused a reduction in Pro-B cells, neutrophils, and granulocytes (Fig. S10). Together, these data suggest that YAP/TAZ deletion from VOPs specifically impaired their communication with embryonic bone-resident endothelial cells through both Cxcl12 signaling and extracellular matrix-mediated interactions and may influence the development of the bone marrow.

Functionally, crosstalk between pericytes and endothelial cells maintains vascular barrier integrity[23]. Osx-conditional YAP/TAZ deletion resulted in abundant extravascular TER119^{+} erythrocytes, which lacked nuclei, indicative of mature red blood cells (Fig. 5G,H, Fig. S11). Comparatively, the majority of TER119^{+} erythrocytes in WT^{Osx} and WT$^{f/f}$ were inside blood vessels in the primary ossification center. This likely indicates a functional role for YAP/TAZ signaling in VOPs in maintenance of vessel barrier function and may also be contributed to by erythropoiesis.

In embryonic bone, VOPs spatially associate with type H vessels. We next asked whether YAP and TAZ mediated the spatial coupling of Osx-expressing precursors with endothelial cells. YAP/TAZ deletion significantly increased the distance from a given Osx-GFP$^+$ cell to its nearest Endomucin$^+$ vessel (Fig. 6A–B, Fig. S12) and significantly altered the proximity distribution in the primary ossification center (Fig. 6C, D). YAP/TAZ deletion doubled the mean (± standard deviation) distance of Osx-GFP$^+$ cells to their nearest blood vessel from 17.4±0.6 μm (WT^{Osx}) to 36.1±8.8 μm (cKO^{Osx}) (Fig. 6D).

This shift in proximity distribution can be potentially explained by 1) a reduced attraction of Osx-GFP$^+$ cells to endothelial cells, 2) a reduced number of Osx-GFP$^+$ cells, or 3) impaired vessel distribution. To control for these factors, we computationally varied spatial Osx-GFP$^+$ cell position and number within each blood vessel map. To test for reduced attraction, we randomized the position of each Osx-GFP$^+$ cell in the extravascular space of its respective POC. If YAP/TAZ deletion impaired attraction independent of cell number or vessel distribution, randomizing the position would collapse the cumulative distribution curves. However, randomizing Osx-GFP+ cell position alone had no effect (Fig. S11D–F). Second, to test for the effect of reduced numbers of Osx-GFP$^+$ cells, independent of vessel morphology, we distributed a fixed number (400) of Osx-GFP+ cells randomly in the extravascular space of each sample's respective primary ossification center. If a reduction in cell density alone explained the distributions, randomizing a fixed number of cells would collapse the cumulative distribution curves. However, fixing Osx-GFP+ cell number also had no effect (Fig. S11G–I). This suggests the differences in distribution arose from altered vessel morphology. To test this, we computed the distance between every extravascular pixel to its nearest vessel. If the vessel morphology was determinative of the proximity distributions, then the proximity distributions of every extravascular pixel would be equivalent to the measured distributions. This was the case (Fig. S11J–L), indicating that Osx-conditional YAP/TAZ deletion alters the formation of the endothelial blood vessel network, and consequently the proximity distribution. Consistently, Osx-conditional YAP/TAZ deletion significantly decreased vessel area fraction and vessel perimeter-to-area ratio (Fig. 6E,F), indicating a small number of larger vessels in the cKO^{Osx} mice. Together, these data suggest that Osx-conditional YAP/TAZ deletion impaired osteoblast precursor-endothelial cell spatial coupling by altering vascular morphogenesis in the embryonic bone.

Based on these functional defects in vascular morphogenesis and identification of Cxcl12 as a putative mediator, we hypothesized that YAP/TAZ signaling promotes vascular morphogenesis via CXCL12. To test this directly in human cells, we used a 3D *in vitro* system, co-culturing GFP-expressing human umbilical vein endothelial cells (HUVECs) and human bone marrow stromal cells (hMSCs) to form tubular vascular networks (Fig. 6G,H, Fig. S13). hMSCs were necessary for neovessel stability and promoted sustainable vascular network formation over 5 days (Fig. 6G,H, Fig. S13). Tubular network formation was significantly impaired by YAP/TAZ depletion from hMSCs (Fig. 6I,J), but was rescued by addition of recombinant CXCL12 (Fig. 6J). These data support a functional role of CXCL12 in YAP/TAZ-mediated angiogenesis.

Endothelial cells mediate cartilage matrix degradation in endochondral development, both directly and indirectly. Directly, anastomotic looping vessels at the chondro-osseous junction

produce matrix metalloproteinases (MMPs, principally MMP9), which degrade cartilage matrix[3]. Osx-conditional YAP/TAZ deletion disrupted the distribution of these vessels across the cartilage septum (Fig. 6K). Therefore, we quantified the density of anastomotic looping vessels in two regions of interest at the chondro-osseous junction: a core region and an outer region (Fig. 6L–M, Fig. S14). Osx-conditional YAP/TAZ deletion significantly altered anastomotic looping vessel density in the core, but not the outer region. Further, *Mmp9*-expressing cells were reduced at the core of the POC but not in the outer edges (Fig. 6N). Indirectly, these growth plate-adjacent vessels also import and support cartilage-degrading cells, including septoclasts and osteoclasts[24,25]. Together, these data suggest that osteoblast precursors spatially regulate vascular invasion and looping vessel morphogenesis at the chondro-osseous junction for growth plate remodeling.

Osx-GFP also targets late hypertrophic chondrocytes[26]. Therefore, to assess chondrocytic YAP/TAZ contributions to growth plate morphogenesis, we explanted limbs for *ex vivo* culture. were isolated at E15.5 and cultured for 6 days, as described previously[27] (Fig. 7A). In contrast to the intact developing limbs, Osx-conditional YAP/TAZ deletion did not impair transverse cartilage septum morphology (Fig. 7B), suggesting that continued vessel invasion is responsible for hypertrophic cartilage remodeling at the chondro-osseous junction during endochondral ossification.

YAP and TAZ mediate mechanoregulation of ex vivo bone formation

Endochondral ossification is regulated by mechanical cues, as seen in fetal akinesia[5], but the underlying mechanisms are unknown. We hypothesized that YAP and TAZ mediate mechanoregulation of development. To test this, we performed bioreactor-based *ex vivo* mechanical stimulation of explanted E15.5 mouse hindlimbs (Fig. 7C). *Ex vivo* mechanical loading increased rudiment mineralization in the hindlimb (Fig. 7D, Fig. S15). To evaluate allele dosage, we additionally evaluated mice with heterozygous deletion of YAP and homozygous deletion of TAZ (YAP cHET^{Osx}/TAZ cKO^{Osx}). Homozygous deletion of both YAP and TAZ abrogated load-induced ALP activity in the primary ossification center (Fig. 7E–G), but not the whole rudiment, in which loading elevated ALP activity regardless of genotype (Fig. 7F,H). While limb explant disrupted the vascular supply, we immunostained for Endomucin to evaluate endothelial cells in the bioreactor. We observed Endomucin^{+} cells in the primary ossification center only in WT limbs exposed to dynamic loading but not in cKO limbs or static loading conditions. However, the observed endothelial cells did not maintain a blood vessel morphology and were not part of a functional vascular network (Fig. S15). To account for contributions of YAP/TAZ deletion to developmental history, we used an orthogonal approach of acute pharmacologic YAP/TAZ inhibition in wild type embryos using Verteporfin[9]. Unlike Osterix-conditional genetic deletion, global YAP/TAZ inhibition abrogated load-induced ALP activity, both in the primary ossification center (Fig. 7I,J) and in the whole limb rudiment (Fig. 7I,K). Thus, Osx-conditional YAP/TAZ deletion, which predominantly altered endochondral bone development in the primary ossification center, also prevented load-induced ALP activity in this region, while acute global inhibition prevented load-induced activity throughout the skeletal rudiment. Together, these data implicate YAP/TAZ mechanosignaling in fetal movement-directed bone development.

Discussion

Here, we establish functional roles of the vessel-associated osteoblast precursors (VOPs) that co-mobilize with blood vessels in fetal endochondral bone development. We show that YAP and TAZ mediate VOP mobilization and function for primary ossification center development. Mechanistically, YAP/TAZ activity in Osterix-expressing cells spatially couples VOPs to blood vessels, coordinates vascular morphogenesis, in part through CXCL12, to regulate growth plate remodeling, and mediates mechanoregulation of fetal bone formation. Together, our findings establish a model of bone development in which VOPs direct angiogenesis, and subsequent endochondral bone development, through YAP/TAZ-*Cxcl12* signaling.

Osteoblast precursors invade the cartilage template prior to endochondral ossification. These cells express the osteogenic transcription factor, Osterix, and mobilize before their differentiation into mature osteoblasts[1]. Here, we show that Osterix-conditional YAP/TAZ deletion impaired osteoblast precursor mobilization and subsequent endochondral bone formation. Limb development features both endochondral ossification in the primary ossification center and intramembranous bone formation in the bone collar[28]. Both are accomplished by osteoblasts, but while the former requires precursor mobilization, the latter occurs by local osteoblast differentiation from perichondrium-resident progenitors[29]. We found that Osterix-conditional YAP/TAZ deletion significantly reduced total cell density and Osx-GFP$^+$ cell density in the primary ossification center, but only moderately reduced either in the bone collar. Previously, we found that YAP and TAZ are required for persistent cell migration via a feedback loop that maintains dynamic cytoskeletal equilibrium[8,12]. Therefore, we performed actin cytoskeleton staining in collagen reporter mice that mark the three primary endochondral cells (chondrocytes, hypertrophic chondrocytes, and osteoblasts), and identified the emergence of osteoblast precursors in the primary ossification center. This osteoblast precursor mobilization was both delayed and reduced by YAP/TAZ deletion. Consistently, YAP/TAZ deletion significantly reduced osteoblast activity, measured by alkaline phosphatase activity, in the primary ossification center, but not in the bone collar. Together, these data show that YAP and TAZ mediate osteoblast precursor mobilization into the primary ossification center and mediate endochondral ossification and implicate distinct functions in endochondral vs. intramembranous ossification.

Endochondral osteoblast precursors co-mobilize with invading blood vessels as VOPs. Here, we show that Osterix-conditional YAP/TAZ deletion impaired osteoblast-lineage cell gene expression, and particularly disrupted angiogenic gene expression in VOPs. Single-cell RNA sequencing confirmed YAP/TAZ-regulated genes in osteoblast-lineage cells that we previously identified in bone and tendon cells (i.e., *Bglap, Bglap2, Mmp9, Mmp14*)[9,30–32]. Notably, YAP/TAZ deletion also significantly reduced *Cxcl12* mRNA in osteoblast-lineage cells. Among fetal osteoblast-lineage cells, *Cxcl12* was primarily expressed by a single sub-cluster. This *Runx2*$^+$, *Pdgfra*$^+$, *Osx*$^+$ population was uniquely marked by expression of *Pdgfrb*$^+$ *and Kitl*$^+$, and additionally moderate *Lepr*$^+$[33], which recent lineage tracing studies identify as vessel-associated osteoblast precursors (VOP)[16,17]. YAP/TAZ deletion particularly altered gene expression in VOPs, relative to other osteoblast-lineage cells. In the VOP cluster, YAP/TAZ deletion reduced expression of *Cxcl12* as well as *Angptl4*, and

increased expression of *Mmp9* and *Mmp13*. Further, YAP/TAZ-dependent VOP-expressed Cxcl12 signaled to Endothelial cell state (c) (putatively type E endothelium) through Cxcr4. *Cxcl12* regulation in VOPs is consistent with recent reports showing that CXCL12 mediates mechanoregulation of vascularized bone formation[34,35]. *Cxcl12* is an angiogenic and myeloid cell-chemotactic chemokine[15] that is expressed by a variety of cell types in adult bone marrow, especially CXCL12-abudant reticular (CAR) cells[36]. However, recent studies show no evidence of CAR cells in embryonic or fetal bone marrow[37,38].

Confirming a functional role for CXCL12 signaling in YAP/TAZ-induced mesenchymal-endothelial crosstalk, we found that recombinant CXCL12 treatment rescued effects of human mesenchymal cell YAP/TAZ depletion on 3D human endothelial cell network formation *in vitro*. Together, this establishes an angiogenic YAP/TAZ-CXCL12 axis in VOPs that couples osteoblast precursor mobilization to vessel morphogenesis. By interrogating existing ChIP-seq datasets we found that YAP and TAZ can localize to the CXCL12 promoter locus, but whether YAP and TAZ regulate *Cxcl12* by direct transcriptional activation or other means in VOPs will require further research beyond the scope of the present study.

Cxcl12 production regulates osteogenic-angiogenic coupling, but is not sufficient to explain all the observed defects in cKO mice. While Osx-conditional YAP/TAZ deletion is perinatal lethal, Prx1- or Osx-conditional deletion of Cxcl12 is not[39]. VOP/endothelial cell co-mobilization can be regulated by both cell intrinsic and cell extrinsic factors. Cell intrinsically, we have previously found that YAP and TAZ regulate cytoskeletal dynamics and subsequent migratory capacity in endothelial cells[8,12], suggesting YAP and TAZ may additionally mediate autonomous VOP mobilization into the primary ossification center. By marking collagen 1-expressing osteoblasts we found that YAP/TAZ deletion doubled phalloidin per cell in the primary ossification center, consistent with our previous studies. Among cell extrinsic factors, extracellular matrix can also influence cell migration. Previously, we also found that Osx-conditional YAP/TAZ deletion profoundly altered collagen matrix content and organization in postnatal bone, resulting in bone fragility[9]. Here, in the embryo, we observed enhanced MMP production in YAP/TAZ cKO fetal limbs that may alter matrix accumulation and organization. Further, analysis of cell-cell communication by CellChat revealed that Osx-conditional YAP/TAZ deletion caused distinct reduction in extracellular matrix-mediated communication between VOPs and endothelial cells, particularly through collagen-integrin interaction. Extracellular matrix interactions have been demonstrated to direct differentiation of type E endothelial cells into the postnatal bone subpopulations[19].

Vessel-associated osteoblast precursors regulate vascular function. PDGFRβ$^+$ vessel stromal cells functionally support blood vessel morphogenesis and vascular barrier function[23]. YAP/TAZ deletion from Osx$^+$/PDGFRβ$^+$ VOPs reduced their spatial association with blood vessels, which spatial variation analysis showed to be driven by dysregulated vessel morphogenesis. These defects in vascular morphogenesis caused two primary functional defects. First, Osx-conditional YAP/TAZ deletion potentially impaired vascular barrier function, possibly through reduced Cxcl12[40], leading to vessel leakiness in the primary ossification center, indicated by extensive erythrocyte extravasation. Erythrocytes

are produced in the bone marrow in adults, such that the accumulation of extravascular erythrocytes is not direct evidence of vessel leakiness. However, unlike in established bone marrow, the extravascular erythrocytes of cKO mice lacked nuclei, suggesting they are terminally differentiated erythrocytes, rather than erythroblasts. This supports a leaky vessel conclusion. Second, Osx-conditional YAP/TAZ deletion impaired hypertrophic cartilage remodeling. Hypertrophic matrix removal is mediated both by cell-autonomous chondrocytic matrix lysis and by degradation at the chondro-osseous junction by cartilage-degrading capillaries and other blood vessel-recruited cells[3,24]. Osx-conditional YAP/TAZ deletion severely impaired cartilage remodeling, lengthening the hypertrophic zone and disrupting the characteristic uniformity of the transverse cartilage septum. Osx-GFP is expressed in both hypertrophic chondrocytes and osteoblast-lineage cells, suggesting both chondrocyte-autonomous and non-autonomous remodeling mechanisms. In a comparable study, Col2-Cre-conditional YAP/TAZ deletion elongated the hypertrophic zone but maintained a flat transverse cartilage septum[41], suggesting that the hypertrophic elongation is hypertrophic chondrocyte-autonomous. In contrast, the conical shape of the cartilage septum correlates with the organization of early vessel invasion[42] and with the disruption of *Mmp9*-expressing cell organization along the chondro-osseous junction. Further, our *ex vivo* limb culture experiments, in which limbs resected from their vascular supply after initiation of the primary ossification center, failed to produce a conical chondro-osseous junction regardless of YAP/TAZ deletion status, suggesting a role for vessel-associated cells in remodeling of the hypertrophic cartilage. Future study will be required to dissect the role of YAP/TAZ signaling crosstalk in the cartilage-degrading capillaries[24,25,43].

Lastly, fetal muscle contractions induce mechanical stimuli that are required for proper bone development. Clinically, fetal akinesia or impaired muscle development, can cause skeletal disorders such as hip dysplasia, arthrogryposis, and impaired bone development[5]. Previously, we and others have investigated the role of mechanical cues in directing skeletal and joint development using both in utero models of disrupted skeletal muscle development[44–50] as well as bioreactor-based mechanical stimulation of explanted fetal limbs ex vivo[27]. These studies demonstrate effects of both frequency and duration of mechanical stimulation on bone and cartilage formation in the fetal limb[51] and form the foundation for the present study. To establish the role of cellular mechanosensation in mechanical load-induced morphogenesis in explanted limbs, we previously used a series of both broad-acting and specific pharmacologic inhibitors against stretch-activated and voltage-gated ion channels[52], including Trpv4[53]. Here, we used this bioreactor system to investigate the mechanotransductive roles of YAP and TAZ in load-induced bone morphogenesis using orthogonal genetic and pharmacologic approaches. YAP and TAZ mediate mechanotransduction in other embryonic tissues[54], and are dysregulated in a mouse model of fetal akinesia[55]. We show that YAP and TAZ mediate mechanical load-induced fetal bone formation ex vivo. In addition to our genetic approach, which may be confounded by developmental history prior to transplant, we used verteporfin to inhibit YAP/TAZ signaling. Verteporfin has cytotoxicity and non-specificity limitations, but serves as an effective control for interpretation of the genetic model. Together, the data suggest that YAP and TAZ mediate mechanoregulation of alkaline phosphatase activity in targeted cells. We did not observe differences in alkaline phosphatase activity between static control and

verteporfin-treated samples, suggesting limited cytotoxicity of verteporfin. Future studies using inducible genetic and alternative pharmacologic agents, including more specific YAP/TAZ inhibitors and inhibitors to upstream mechanotransductive signaling (e.g., Src or Rho inhibitors) will be needed.

Together, these data identify YAP and TAZ as mechanoresponsive transcriptional regulators that couple osteoblast precursor mobilization to vessel morphogenesis and mechano-regulated bone development.

Limitations of the Study

This study has several limitations. First, our study focused only on wildtype and double homozygous knockout mice, and does not inform the relative roles of YAP vs. TAZ. We chose this based on our prior study identifying YAP and TAZ as combinatorial regulators of postnatal bone development, with perinatal lethality only in double homozygous knockout mice[9]. Future study will be required to dissect the respective roles of YAP or TAZ in embryonic bone. Second, we selected Osterix-Cre based on the predominant distribution of YAP/TAZ expression in skeletal-lineage cells[9]. The Osterix-Cre driver has been observed to exhibit a skeletal phenotype in the absence of floxed alleles[56,57]. However, the magnitude of the effect on skeletal development is determined by the genetic background. We controlled for this using both floxed-alone and Cre-containing controls. As we described previously[30,31], the Osx-GFP did not interfere with the effects of YAP/TAZ signaling in these mice. Our work identifies VOP-mediated vessel morphogenesis as a critical regulator of embryonic bone development, but our bioreactor loading experiments identifying YAP and TAZ as mechanotransducers in embryonic bone required limb explants disconnected from the native vascular supply. We observed Endomucin^{+} cells in the primary ossification center of only wildtype limbs exposed to loading, suggesting a potential coupling of mechanoresponsiveness and vascular morphogenesis, consistent with prior studies[58,59]. Future study to enable modulation of *in utero* mechanical stimulation will be required to directly test the roles of YAP and TAZ in mechanoregulation of skeletal morphogenesis *in vivo*.

STAR Methods

RESOURCE AVAILABILITY

Lead contact—Further information and requests for resources and reagents should be directed to and will be fulfilled by the lead contact, Joel Boerckel (boerckel@pennmedicine.upenn.edu)

Materials availability—This study did not generate unique reagents.

Data and code availability

- Single-cell RNA-seq data have been deposited at GEO and are publicly available as of the data of publication. Accession numbers are listed in the key resource table.

- This paper does not report original code. Analysis of the data presented here used published R packages that are available on GitHub. For analysis using published R packages, we used: R v4.1.0, Seurat v4.1.1, and CellChat v1.6.0.
- Any additional information required to reanalyze the data reported in this paper is available from the lead contact upon request

EXPERIMENTAL MODEL AND STUDY PARTICIPANT DETAILS

Animals—We conditionally deleted YAP and TAZ from Osx1-expressing cells ($YAP^{fl/fl}$;$TAZ^{fl/fl}$;Osx1-GFP::Cre) comparison to littermate wild type ($YAP^{fl/fl}$;$TAZ^{fl/fl}$) and Osx1-GFP::Cre wild type ($YAP^{WT/WT}$; $TAZ^{WT/WT}$;Osx1-GFP::Cre) controls with a mixed C57BL/6 background[9,26]. Additionally, we used mice in which we conditionally deleted YAP and TAZ from Osx1-expressing cells ($YAP^{fl/fl}$;$TAZ^{fl/fl}$;Osx1-GFP::Cre) comparison to littermate wild type ($YAP^{fl/fl}$;$TAZ^{fl/fl}$), but also included a transgenic fluorescent reporter under control of the 3.6kb fragment of the Collagen1a1 promoter, marked by CFP (Col1(3.6)-CFP). Additionally, we used a triple transgenic fluorescent reporter model which co-expresses fluorescent proteins under the control of promoters for three collagen genes: Collagen II, marked by CFP (Col2-CFP); Collagen X, by mCherry (ColX-mCherry); and the 3.6kb fragment of the Collagen1a1 promoter, by YPF (Col1-YFP)[60]. The Col1-YFP is expressed in both immature and committed osteoblasts. To generate embryos by timed pregnancies, breeding pairs were housed together for a single night and pregnancy was determined by visual inspection and increased female weight gain over the course of the pregnancy. To generate YAP/TAZ $cKO^{osx}/WT^{fl/fl}$ littermate embryos, a YAP/TAZ cKO^{osx} stud male was housed with a $WT^{fl/fl}$ female overnight, which was never exposed to doxycycline. To generate WT^{osx} embryos, a WT^{osx} stud male was housed with a $YAP^{WT/WT}$;$TAZ^{WT/WT}$ female overnight. Pregnant mice were euthanized by CO_2 and secondary cervical dislocation and embryos were harvested at 15.5 days (E15.5) and 17.5 days (E17.5) post-conception. Mice were genotyped by an external service (Transnetyx, Cordova, TN, USA). All animals were fed regular chow ad libitum. All animals were housed in cages containing 2–5 animals each, with the exception that stud males were housed alone after they had been selected as stud males. Mice were maintained at constant 25°C on a 12h light-dark cycle. All procedures were performed with IACUC approval (protocol: 806281).

Cells—GFP+ HUVECs (Angio-Proteomie) were expanded in human endothelial growth medium with 5% FBS (EGM-SF1; Angio-Proteomie, Boston, AM, USA) in cell culture flasks coated with 0.2% gelatin (Sigma Aldrich). hMSCs were cultured in RoosterNourish™-MSC-XF (both RoosterBio). All cells were cultured at 37°C.

METHOD DETAILS

Histology and immunofluorescence—For cryohistological analysis, embryos were fixed for 24–48 hours in 4% PFA (Fisher) in water at 4°C. Only samples fixed for similar times were compared. Following fixation, samples were saturated in 30% sucrose/PBS at 4°C and embedded in OCT (Fisher). Samples embedded in OCT were stored at −20°C until further use. 7 μm sections were generated by cryohistology (NX70 cryostat Thermo Fisher Scientific), using methods previously described[60]. For immunocytochemistry, tissue

sections were washed 3× 5 mins with PBS. Then, samples were permeabilized and blocked for 1hr at RT with blocking buffer (PBS/ 5% goat serum/ 0.3% Triton X-100 (MP Biomedical). Following this, cells were stained with primary antibodies overnight at 4°C in a dilution buffer (PBS/ 0.01%BSA/ 0.3% Triton): YAP (1:100, D8H1X #14074 Cell Signaling Technology), TAZ/WWTR1 (1:100, PA1-46190 Invitrogen), Collagen-10 (1:100, ab58632 Abcam), GFP (1:1000, ab13970 Abcam), Endomucin (1:50, sc-65495 Santa Cruz), Ter119-APC (1:100, BioLegend 116211). The next day, samples were washed 3× 5 mins with PBS and then stained with corresponding secondary antibodies (1:1000; 4414S Cell Signaling Technology, 8889S Cell Signaling Technology, A21247 Life Tech). F-actin was stained with Alexa Fluor-conjugated Phalloidin (1:40, Invitrogen Thermo Fisher Scientific) for 2hr. Alkaline Phosphatase was stained with the Vector blue Alkaline phosphatase substrate kit (Vector SK-5300), per manufacturer's instructions. Sections were stained with Calcein blue, according to Dyment et al[60]. Following staining, samples were mounted in Prolong Diamond (Invitrogen Thermo Fisher Scientific) or 50% glycerol/PBS. RNAscope was performed according to Advanced Cell Diagnostics manufacturer's instructions.

Histological imaging and analysis—Fluorescent images were captured with an Axioscan (Carl Zeiss Microscopy Deutschland GmbH). Data acquisition was performed with ZEN imaging suite (Zeiss). Image analysis (cell density, morphometric measurements, fluorescent intensity, and coordinate values) were performed with ImageJ (FIJI)[61]. Primary ossification center, bone collar, and hypertrophic zone regions of interest were determined manually by darkfield tissue morphology and additionally informed by relevant immunofluorescent stains (e.g. Collagen-10). ROIs were managed with the ImageJ's built-in ROI-Manager. The cell number within each ROI was determined manually with the Cell Counter Plugin in ImageJ and DAPI signal. The line plots of fluorescent intensity (Fig. 2B,C) were generated from the average intensity of 20–30 μm width bins orthogonal to the central axis along the bone rudiment. Each average fluorescent intensity measurement was normalized to the area in which that measurement was taken. For the Col2-CFP, Col10-RFP, Col1(3.6kb)-YFP line plot analysis, the area-normalized fluorescent intensity of each channel in a region with external to the tissue was subtracted from the area-normalized tissue intensity. To quantify the distance between Osx-GFP$^+$ cells and Endomucin$^+$ vessels (Fig. 5C,D), we generated maps of coordinates for GFP$^+$ cell positions and vessel positions in each primary ossification center. We used R to determine the nearest vessel to each GFP$^+$ cell position. Further, to evaluate different explanations for the proximity distributions, we computationally varied the spatial position of each Osx-GFP+ cell within the primary ossficiation center. To account for the contribution of Osx-GFP+ cell-endothelial cell attraction, we took the Endomucin+ vessel map from both WT and cKO samples and then randomly distributed the Osx:GFP+ cells within that sample (Fig S15). Thus, if Osx-GFP$^+$ cell-endothelial cell attraction explained the proximity distribution, then randomizing the distribution of Osx-GFP+ cells should produce equivalent proximity distributions in both WT and cKO samples. To account for the contribution of Osx-GFP+ cell number, we took the Endomucin+ vessel map from both WT and cKO samples and then randomly distributed an equivalent number of Osx-GFP+ cells (Fig S15). Thus, if the reduced number of Osx-GFP$^+$ cells explained the proximity distribution, then randomly distributing an equivalent number of Osx-GFP+ cells to both WT and cKO vessel maps should produce

equivalent proximity distributions. To account for the contribution of vessel distribution, for any possible Osx-GFP$^+$ cell position, we took the Endomucin$^+$ vessel map from both WT and cKO samples and mapped the proximity distribution of all extravascular pixels in the primary ossification center (Fig S15). Looping vessels were calculated as Endomucin+ vessels within 50 μm of the chondro-osseous interface. For bioreactor analysis, during image quantification of regions of interest, samples were excluded if the whole limb rudiment was not intact or if the primary ossification center-bone collar interface was unclear.

Tissue preparation for scRNA-sequencing—Timed pregnancies and mouse embryos were generated, as described above. For tissue isolation, embryonic forelimbs were isolated on ice and trimmed to removed excess and loose skin/soft tissue and the paw. Individual embryonic tails or yokesacs were placed aside for genotyping. A single-cell suspension was isolated as previously described[14], in the presence of the transcriptional inhibitor Actinomycin D (MP Biomedicals). Briefly, cells from individual samples were disassociated from the tissue with a digestion media including DMEM, fetal bovine serum (Sigma), Collagenase II (Gibco Thermo Fisher Scientific), Pronase (Sigma Aldrich), and Actinomycin D (2 μg/ml) for 75 minutes at 37°C. Following, cells were washed with PBS/0.01% BSA and passed through 70 μm cell strainers. Then, red blood cells were lysed with a Red Blood Cell Lysis kit (Miltenyi Biotec, 130-094-183), per manufacturer instructions. Dead cells were then removed with a Dead Cell Removal kit (Miltenyi Biotec 130-090-101) and MACS MS columns (Miltenyi Biotec), and a MiniMACS Magnetic Cell Separator (Miltenyi Biotec). Following dead cell removal, each sample was confirmed to have >95% viability. To allow time for genotyping, cells were then processed according to 10x Genomics ‘Methanol Fixation of Cells for Single-cell RNA Sequencing protocol, Rev D’. Cell suspensions were resuspended per 10x Genomics ‘Methanol Fixation of Cells for Single-cell RNA Sequencing protocol, Rev D’ and processed for sequencing.

Single-cell RNA sequencing and analysis—Next-generation sequencing libraries were prepared using the 10x Genomics Chromium Single-cell 3’ Reagent kit v3 per manufacturer’s instructions. Libraries were uniquely indexed using the Chromium Index Kit, pooled, and sequenced on an Illumina NovaSeq 6000 sequencer in a paired-end run. Sequencing for each library targeted 77,000 mean reads per cell. Data was then processed using the Cell Ranger pipeline (10x Genomics, v.6.0.0) for demultiplexing and alignment of sequencing reads to the mm10 transcriptome and creation of feature-barcode matrices. For further analysis, we used Seurat v4[62]. Cells with less than 600 genes, greater than 6000 genes, or those with greater than 5% mitochondrial reads were removed. Data from individual samples were LogNormalized. We identified 2000 variable features across each sample. Samples were integrated using the Seurat alignment method for data integration[63]. Samples were scaled using ScaleData. Linear dimensional reduction was conducted using principal component analysis (PCA). The entire 120,292-cell dataset was projected onto two-dimensional space using UMAP, and the data were clustered using Louvain clustering. The analyses on the whole limb used 50 PCA dimensions and a resolution of 2.5. The FindAllMarkers function and canonical marker genes was used to identify major cell types. The 77 clusters identified by Louvain clustering were merged based on similar expression patterns into 12 distinct major cell populations. Osteoblasts constituted only 1 of the initial

77 clusters. These cells were subsetted and rerun through the above pipeline. The analysis of the osteoblasts used 15 PCA dimensions and a resolution of 0.5. The iterative clustering of the osteoblasts revealed 7 cell states, which were identified using the FindAllMarkers function and cell state specific markers determined in prior lineage tracing studies. For gene set enrichment analysis (GSEA), a pre-ranked list of the genes was constructed by fold change between comparisons and evaluated with GSEA v4.2.3. Significant inter-cluster gene expression differences between genotypes was determined by MAST with Bonferroni corrections. Each wildtype was separately compared by MAST with Bonferroni corrections to the Osx-conditional YAP/TAZ knockout samples. Additionally, endothelial cells and chondrocytes were subsetted and rerun through the above pipeline. The analysis of the endothelial cells used 15 PCA dimensions and a resolution of 0.2. Clusters which were mostly likely to contain type H endothelial cells were determined by their comparative expression of *Emcn* and *Pecam1*. The analysis of the chondrocytes used 8 PCA dimensions and a resolution of 0.5. Cell-cell communication analysis was done with the package CellChat[21], which accounts for ligand and receptor expression, as well as co-expression of genes that are agonistic and antagonistic to a particular communication pathway. Cell-cell communication analysis via CellChat was performed on the entire osteoblast and endothelial cell populations and specifically between vessel-associated osteoblast precursors and type H endothelial cells. Immune cell populations were identified using the automated cell identification package, ScType[64].

Analysis of published ChIPseq—Fastq files were downloaded from the Gene Expression Omnibus (accession number GSE163458). Raw data were trimmed of adapter contamination using Cutadapt[65]. They were aligned to GRCh38/hg38 using bowtie2[66]. After removing mitochondrial reads, PCR duplicates were removed with Picard. Peaks were called with MACS2 using the input file as background, with an FDR q-value cutoff of 0.01[67]. Input-subtracted bigWig files were made with bedtools, genomeCoverageBed, and bedGraphtoBigWig[68]. Browser tracks were visualized using the UCSC Genome Browser[69].

3D in vitro vascular network assay—GFP+ HUVECs (Angio-Proteomie) were expanded in human endothelial growth medium with 5% FBS (EGM-SF1; Angio-Proteomie, Boston, AM, USA) in cell culture flasks coated with 0.2% gelatin (Sigma Aldrich). hMSCs were cultured in RoosterNourish™-MSC-XF (both RoosterBio). For RNAi YAP and TAZ knock down – hMSCs were starved for 6h in DMEM without antibiotics before adding siRNA for YAP or TAZ and scramble control (Stealth RNAi Invitrogen Thermo Fisher Scientific) in OptiMEM with addition of Lipofectamine 3000 (both Thermo Fisher Scientific). GFP+ HUVECs and hMSCs were embedded (4:1; total final cell concentration 2 Mio cells/mL) in photocrosslinked gelatin-fibrin hydrogels (CELLINK) composed of 5% GelMA, 5 mg/ml fibrinogen and 0.2% LAP for photoinitiation and cultivated in vitro for up to 5 days with endothelial basal medium containing 0.1% FBS and 1% P/S (Thermo Fisher Scientific). For rescue experiment, 100 ng/mL recombinant CXCL12/SDF-1 (350-NS/CF; R&D Systems) was added to the medium. Images were taken at 5 days using a Keyence BZ-X800 Fluorescence Microscope (Keyence). All images were blinded for group and treatment. The tube number and mean tube length were analyzed using Fiji ImageJ. The area to be analyzed was defined as the full area of the hydrogel

which was visible in the images. To correct for differences in analyzed area (ROI) dimension between the hydrogels, the tube number was normalized to the analyzed area (ROI). Finally, the normalized tube number and the absolute mean tube length were calculated relative to the respective scramble control. To establish the assay we performed two independent experiments: In experiment 1, we used two different MSC lines combined with two different HUVEC lines with 2–3 replicates per MSC/HUVEC combination and condition. Experiment 2 was used to replicate and strengthen the data with one MSC/HUVEC combination and 4 replicates for each condition (biological replicates n= 5; technical replicates total n= 7–11). For the knockout and rescue experiment, we combined the data from two independent experiments – experiment 1 established the knockout with one MSC/HUVEC combination and 4 replicates for each condition. In the second experiment, we used two different MSC lines combined with one HUVEC line testing 2–3 replicates per MSC/HUVEC combination and condition and performed the rescue experiment (biological replicates n= 2–3; technical replicates total n= 6–11).

***Ex vivo* bioreactor experiments—**We explanted hindlimbs at E15.5 and cultured them in either dynamically loaded or static conditions in osteogenic media containing: αMEM, 1% Pen/Strep, GlutaMAX, 100μM Ascorbic acid (Sigma Aldrich) for 5–6 days. Soft tissue was first removed from the hindlimbs. The limb explants were pinned at the hip to a polyurethane deformable foam (Sydney Heath & Son) and positioned in a mechanostimulation bioreactor (Ebers TC-3). Dynamic loading was applied at the top of the foam at 0.67 Hz for 2h, 3x/day, producing cyclic knee flexion to 14±4°, which mimics motion produced through prenatal muscle contractions. Static conditions used the same set up but without dynamic loading. We evaluated the effect of loading on hindlimb explants cultured under static or dynamic conditions for 5 days. After culture, the limbs were evaluated by Optical Projection Tomography (OPT). For OPT, hindlimbs were dehydrated and stained for cartilage and mineralized tissue using alcian blue and alizarin red S, as previously described[45]. Stained and fixed limbs were embedded in agarose, dehydrated and cleared in a solution of BABB in preparation for 3D imaging using OPT, according to Quintana and Sharpe[70]. Limbs were scanned under visible light to obtain 3D images of the alcian blue staining (cartilage) and under the Texas-red filter to obtain auto-fluorescent 3D images of the alizarin red S-stained region (the mineralized region). Scans were reconstructed using NRecon (SkyScan, Bruker microCT, 2011). For the genetic knockout, E15.5 embryos were generated for 3 rounds of bioreactor experiments, as described above. In prior studies, Osx-conditional YAP/TAZ deletion impaired postnatal bone development in an allele-dependent manner. To consider a moderate loss in mechanotransduction, here we evaluated $WT^{f/f}$;$WT^{f/f}$, YAP $cHET^{Osx}$/TAZ cKO^{Osx}, and YAP/TAZ cKO^{Osx} embryos, as described previously for postnatal mice[9]. To generate these samples, $YAP^{f/f}$; $TAZ^{f/f}$ females were bred with $YAP^{f/+}$; $TAZ^{f/f}$; Osx-cre stud males. Following culture, samples were processed for cryohistology in the method described above. The fluorescent intensity of samples was normalized to average dynamic wildtype of their respective round to account for variations between rounds. Growth plate morphology was quantified in limb explants under the static condition. For pharmacologic inhibition, C57BL/6J E15.5 hindlimbs were isolated. Limbs were preprocessed for culture in the above way. Limbs were cultured under

dynamic or static conditions in osteogenic media and in the presence of 5mM verteporfin or a vehicle control (DMSO).

Schematics—The cartoons in Fig. 3A, 7A, and 7C were created using BioRender.com

QUANTIFICATION AND STATISTICAL ANALYSIS

Statistical analysis—GraphPad Prism V.8 and V.9 were used for statistical analysis. Comparisons between two groups were evaluated by Student's t-test and multiple-group comparisons were evaluated by 1- or 2-way ANVOA with post hoc analysis by Tukey's HSD and Sidek's multiple comparisons, respectively. Normality of data distributions were assessed by D'Agostino-Pearson omnibus normality test and homoscedastic according to Bartlett's test. When parametric test assumptions were not met, data were log transformed, and residuals were re-evaluated prior to parametric analysis. Single-cell RNA sequencing statistics are discussed in the associated methods section above. A p-value < 0.05 was considered statistically significant. Sample sizes are indicated in the figure legends. Where possible data is displayed with the individual samples shown. Asterisks represent significant differences with a p-value < 0.05. Multiple asterisks represent lower p-values, as indicated in the figure legend. Sample sizes indicate measurements of individual embryos.

Supplementary Material

Refer to Web version on PubMed Central for supplementary material.

Acknowledgements

The authors would like to thank the Boerckel lab for constructive discussions, Dr. Robert Tower (UTSW) for helpful suggestions, Dr. Farshid Guilak for providing protocols for embryonic forelimb cell isolation, Dr. Sierra Collins for assistance with ChIPseq analysis, and the Children's Hospital of Philadelphia Center for Applied Genomics for their assistance with scRNA-seq sample processing.

Funding:

NIH/NIAMS: R01 AR073809, R01 AR074948, P30AR069619, 5T32AR007132 (to JMC), NSF CMMI 1548571 (to JDB), ERC Grant agreement (number 336306). The development of the vascular network assay was funded by the Alternatives Research and Development Foundation (to NN, JDB, AL, RLG). AL received a Research Fellowship funded by the Deutsche Forschungsgemeinschaft (DFG; project no.: 440525257; reference: LA 4007/2-1).

Data and materials availability:

All data associated with this study are present in the paper or the Supplementary Materials. Sequencing data have been deposited in GEO (GSE227818). Published ChIP seq data set is under accession code GSE163458.

References and Notes

1. Maes C et al. Osteoblast precursors, but not mature osteoblasts, move into developing and fractured bones along with invading blood vessels. Dev. Cell 19, 329–344 (2010). [PubMed: 20708594]
2. Kusumbe AP, Ramasamy SK & Adams RH Coupling of angiogenesis and osteogenesis by a specific vessel subtype in bone. Nature 507, 323–328 (2014). [PubMed: 24646994]

3. Romeo SG et al. Endothelial proteolytic activity and interaction with non-resorbing osteoclasts mediate bone elongation. Nat. Cell Biol 21, 430–441 (2019). [PubMed: 30936475]
4. Shen B et al. A mechanosensitive peri-arteriolar niche for osteogenesis and lymphopoiesis. Nature 591, 438–444 (2021). [PubMed: 33627868]
5. Nowlan NC Biomechanics of foetal movement. Eur. Cell. Mater 29, 1–21; discussion 21 (2015). [PubMed: 25552425]
6. Verbruggen SW et al. Stresses and strains on the human fetal skeleton during development. J. R. Soc. Interface 15, 20170593 (2018). [PubMed: 29367236]
7. Dupont S et al. Role of YAP/TAZ in mechanotransduction. Nature 474, 179–183 (2011). [PubMed: 21654799]
8. Mason DE et al. YAP and TAZ limit cytoskeletal and focal adhesion maturation to enable persistent cell motility. J. Cell Biol 218, 1369–1389 (2019). [PubMed: 30737263]
9. Kegelman CD et al. Skeletal cell YAP and TAZ combinatorially promote bone development. FASEB J 32, 2706–2721 (2018). [PubMed: 29401582]
10. Xiong J, Almeida M & O'Brien CA The YAP/TAZ transcriptional co-activators have opposing effects at different stages of osteoblast differentiation. Bone 112, 1–9 (2018). [PubMed: 29626544]
11. Kegelman CD, Collins JM, Nijsure MP, Eastburn EA & Boerckel JD Gone Caving: Roles of the Transcriptional Regulators YAP and TAZ in Skeletal Development. Curr. Osteoporos. Rep 18, 526–540 (2020). [PubMed: 32712794]
12. Mason DE et al. Mechanotransductive feedback control of endothelial cell motility and vascular morphogenesis http://biorxiv.org/lookup/doi/10.1101/2022.06.15.496293 (2022) doi:10.1101/2022.06.15.496293.
13. Zhong L et al. Single cell transcriptomics identifies a unique adipose lineage cell population that regulates bone marrow environment. eLife 9, e54695 (2020). [PubMed: 32286228]
14. Kelly NH, Huynh NPT & Guilak F Single cell RNA-sequencing reveals cellular heterogeneity and trajectories of lineage specification during murine embryonic limb development. Matrix Biol 89, 1–10 (2020). [PubMed: 31874220]
15. Janssens R, Struyf S & Proost P The unique structural and functional features of CXCL12. Cell. Mol. Immunol 15, 299–311 (2018). [PubMed: 29082918]
16. Sivaraj KK et al. Regional specialization and fate specification of bone stromal cells in skeletal development. Cell Rep 36, 109352 (2021). [PubMed: 34260921]
17. Böhm A-M et al. Activation of Skeletal Stem and Progenitor Cells for Bone Regeneration Is Driven by PDGFRβ Signaling. Dev. Cell 51, 236–254.e12 (2019). [PubMed: 31543445]
18. Ong YT et al. A YAP/TAZ-TEAD signalling module links endothelial nutrient acquisition to angiogenic growth. Nat. Metab 4, 672–682 (2022). [PubMed: 35726026]
19. Langen UH et al. Cell-matrix signals specify bone endothelial cells during developmental osteogenesis. Nat. Cell Biol 19, 189–201 (2017). [PubMed: 28218908]
20. Rodrigues J et al. Oestrogen enforces the integrity of blood vessels in the bone during pregnancy and menopause. Nat. Cardiovasc. Res 1, 918–932 (2022). [PubMed: 36531334]
21. Jin S et al. Inference and analysis of cell-cell communication using CellChat. Nat. Commun 12, 1088 (2021). [PubMed: 33597522]
22. Greenbaum A et al. CXCL12 in early mesenchymal progenitors is required for haematopoietic stem-cell maintenance. Nature 495, 227–230 (2013). [PubMed: 23434756]
23. Lindahl P, Johansson BR, Levéen P & Betsholtz C Pericyte loss and microaneurysm formation in PDGF-B-deficient mice. Science 277, 242–245 (1997). [PubMed: 9211853]
24. Sivaraj KK et al. Mesenchymal stromal cell-derived septoclasts resorb cartilage during developmental ossification and fracture healing. Nat. Commun 13, 571 (2022). [PubMed: 35091558]
25. Tosun B, Wolff LI, Houben A, Nutt S & Hartmann C Osteoclasts and Macrophages—Their Role in Bone Marrow Cavity Formation During Mouse Embryonic Development. J. Bone Miner. Res 37, 1761–1774 (2022). [PubMed: 35689447]

26. Rodda SJ & McMahon AP Distinct roles for Hedgehog and canonical Wnt signaling in specification, differentiation and maintenance of osteoblast progenitors. Dev. Camb. Engl 133, 3231–3244 (2006).
27. Chandaria VV, McGinty J & Nowlan NC Characterising the effects of in vitro mechanical stimulation on morphogenesis of developing limb explants. J. Biomech 49, 3635–3642 (2016). [PubMed: 27743631]
28. Debnath S et al. Discovery of a periosteal stem cell mediating intramembranous bone formation. Nature 562, 133–139 (2018). [PubMed: 30250253]
29. Ono N, Balani DH & Kronenberg HM Stem and progenitor cells in skeletal development. Curr. Top. Dev. Biol 133, 1–24 (2019). [PubMed: 30902249]
30. Kegelman CD et al. YAP and TAZ Promote Periosteal Osteoblast Precursor Expansion and Differentiation for Fracture Repair. J. Bone Miner. Res 36, 143–157 (2021). [PubMed: 32835424]
31. Kegelman CD et al. YAP and TAZ Mediate Osteocyte Perilacunar/Canalicular Remodeling - Kegelman - 2020 - Journal of Bone and Mineral Research - Wiley Online Library. J. Bone Miner. Res 35, 196–210 (2020). [PubMed: 31610061]
32. Jones DL et al. Mechanoepigenetic regulation of extracellular matrix homeostasis via Yap and Taz. Proc. Natl. Acad. Sci 120, e2211947120 (2023). [PubMed: 37216538]
33. Zhou BO, Yue R, Murphy MM, Peyer JG & Morrison SJ Leptin-receptor-expressing mesenchymal stromal cells represent the main source of bone formed by adult bone marrow. Cell Stem Cell 15, 154–168 (2014). [PubMed: 24953181]
34. Bosch-Marce M et al. Effects of Aging and Hypoxia-Inducible Factor-1 Activity on Angiogenic Cell Mobilization and Recovery of Perfusion After Limb Ischemia. Circ. Res 101, 1310–1318 (2007). [PubMed: 17932327]
35. Leucht P et al. CXCR4 antagonism attenuates load-induced periosteal bone formation in mice. J. Orthop. Res 31, 1828–1838 (2013). [PubMed: 23881789]
36. Sugiyama T, Kohara H, Noda M & Nagasawa T Maintenance of the hematopoietic stem cell pool by CXCL12-CXCR4 chemokine signaling in bone marrow stromal cell niches. Immunity 25, 977–988 (2006). [PubMed: 17174120]
37. Hall TD et al. Murine fetal bone marrow does not support functional hematopoietic stem and progenitor cells until birth. Nat. Commun 13, 5403 (2022). [PubMed: 36109585]
38. Liu Y et al. A specialized bone marrow microenvironment for fetal haematopoiesis. Nat. Commun 13, 1327 (2022). [PubMed: 35288551]
39. Tzeng Y-S et al. Imbalanced Osteogenesis and Adipogenesis in Mice Deficient in the Chemokine Cxcl12/Sdf1 in the Bone Mesenchymal Stem/Progenitor Cells. J. Bone Miner. Res. Off. J. Am. Soc. Bone Miner. Res 33, 679–690 (2018).
40. Döring Y et al. Vascular CXCR4 Limits Atherosclerosis by Maintaining Arterial Integrity. Circulation 136, 388–403 (2017). [PubMed: 28450349]
41. Vanyai HK et al. Control of skeletal morphogenesis by the Hippo-YAP/TAZ pathway. Dev. Camb. Engl 147, dev187187 (2020).
42. Langen UH et al. Cell-matrix signals specify bone endothelial cells during developmental osteogenesis. Nat. Cell Biol 19, 189–201 (2017). [PubMed: 28218908]
43. Sivaraj KK et al. YAP1 and TAZ negatively control bone angiogenesis by limiting hypoxia-inducible factor signaling in endothelial cells. eLife 9, e50770 (2020). [PubMed: 31958058]
44. Sotiriou V, Huang Y, Ahmed S, Isaksson H & Nowlan NC Prenatal murine skeletogenesis partially recovers from absent skeletal muscle as development progresses. Eur. Cell. Mater 44, 115–132 (2022). [PubMed: 36345651]
45. Sotiriou V, Rolfe RA, Murphy P & Nowlan NC Effects of Abnormal Muscle Forces on Prenatal Joint Morphogenesis in Mice. J. Orthop. Res 37, 2287–2296 (2019). [PubMed: 31297860]
46. Kahn J et al. Muscle contraction is necessary to maintain joint progenitor cell fate. Dev. Cell 16, 734–743 (2009). [PubMed: 19460349]
47. Sharir A, Stern T, Rot C, Shahar R & Zelzer E Muscle force regulates bone shaping for optimal loadbearing capacity during embryogenesis. Development 138, 3247–3259 (2011). [PubMed: 21750035]

48. Nowlan NC, Dumas G, Tajbakhsh S, Prendergast PJ & Murphy P Biophysical stimuli induced by passive movements compensate for lack of skeletal muscle during embryonic skeletogenesis. Biomech. Model. Mechanobiol 11, 207–219 (2012). [PubMed: 21505895]
49. Nowlan NC et al. Developing bones are differentially affected by compromised skeletal muscle formation. Bone 46, 1275–1285 (2010). [PubMed: 19948261]
50. Pierantoni M et al. Muscular loading affects the 3D structure of both the mineralized rudiment and growth plate at early stages of bone formation. Bone 145, 115849 (2021). [PubMed: 33454374]
51. Khatib N, Parisi C & Nowlan NC Differential effect of frequency and duration of mechanical loading on fetal chick cartilage and bone development. Eur. Cell. Mater 41, 531–545 (2021). [PubMed: 34033115]
52. Parisi C, Chandaria VV & Nowlan NC Blocking mechanosensitive ion channels eliminates the effects of applied mechanical loading on chick joint morphogenesis. Philos. Trans. R. Soc. B Biol. Sci 373, 20170317 (2018).
53. Khatib NS et al. Mechanoregulatory role of TRPV4 in prenatal skeletal development. Sci. Adv 9, eade2155 (2023). [PubMed: 36696489]
54. Abuwarda H & Pathak MM Mechanobiology of neural development. Curr. Opin. Cell Biol 66, 104–111 (2020). [PubMed: 32687993]
55. Shea CA, Rolfe RA, McNeill H & Murphy P Localization of YAP activity in developing skeletal rudiments is responsive to mechanical stimulation. Dev. Dyn 249, 523–542 (2020). [PubMed: 31747096]
56. Chen J et al. Osx-Cre Targets Multiple Cell Types besides Osteoblast Lineage in Postnatal Mice. PLOS ONE 9, e85161 (2014). [PubMed: 24454809]
57. Huang W & Olsen BR Skeletal Defects in Osterix-Cre Transgenic Mice. Transgenic Res 24, 167–172 (2015). [PubMed: 25139670]
58. Boerckel JD, Uhrig BA, Willett NJ, Huebsch N & Guldberg RE Mechanical regulation of vascular growth and tissue regeneration in vivo. Proc. Natl. Acad. Sci. U. S. A 108, E674–680 (2011). [PubMed: 21876139]
59. Ruehle MA et al. Extracellular matrix compression temporally regulates microvascular angiogenesis. Sci. Adv 6, eabb6351 (2020). [PubMed: 32937368]
60. Dyment NA et al. High-Throughput, Multi-Image Cryohistology of Mineralized Tissues. J. Vis. Exp. JoVE (2016) doi:10.3791/54468.
61. Schindelin J et al. Fiji: an open-source platform for biological-image analysis. Nat. Methods 9, 676–682 (2012). [PubMed: 22743772]
62. Hao Y et al. Integrated analysis of multimodal single-cell data. Cell 184, 3573–3587.e29 (2021). [PubMed: 34062119]
63. Stuart T et al. Comprehensive Integration of Single-Cell Data. Cell 177, 1888–1902.e21 (2019). [PubMed: 31178118]
64. Ianevski A, Giri AK & Aittokallio T Fully-automated and ultra-fast cell-type identification using specific marker combinations from single-cell transcriptomic data. Nat. Commun 13, 1246 (2022). [PubMed: 35273156]
65. Martin M Cutadapt removes adapter sequences from high-throughput sequencing reads. EMBnet.journal 17, 10–12 (2011).
66. Langmead B & Salzberg SL Fast gapped-read alignment with Bowtie 2. Nat. Methods 9, 357–359 (2012). [PubMed: 22388286]
67. Zhang Y et al. Model-based Analysis of ChIP-Seq (MACS). Genome Biol 9, R137 (2008). [PubMed: 18798982]
68. Quinlan AR & Hall IM BEDTools: a flexible suite of utilities for comparing genomic features. Bioinformatics 26, 841–842 (2010). [PubMed: 20110278]
69. Kent WJ et al. The human genome browser at UCSC. Genome Res 12, 996–1006 (2002). [PubMed: 12045153]
70. Quintana L & Sharpe J Preparation of Mouse Embryos for Optical Projection Tomography Imaging. Cold Spring Harb. Protoc 2011, pdb.prot5639 (2011).

Highlights

- Osx-conditional deletion of YAP and TAZ impairs fetal bone development
- YAP and TAZ mediate vessel-associated osteoblast precursor (VOP)-blood vessel co-mobilization and morphogenesis
- YAP and TAZ regulate *Cxcl12* expression in Pdgfrβ^{+} VOPs
- YAP and TAZ regulate load-induced osteogenesis during fetal bone development

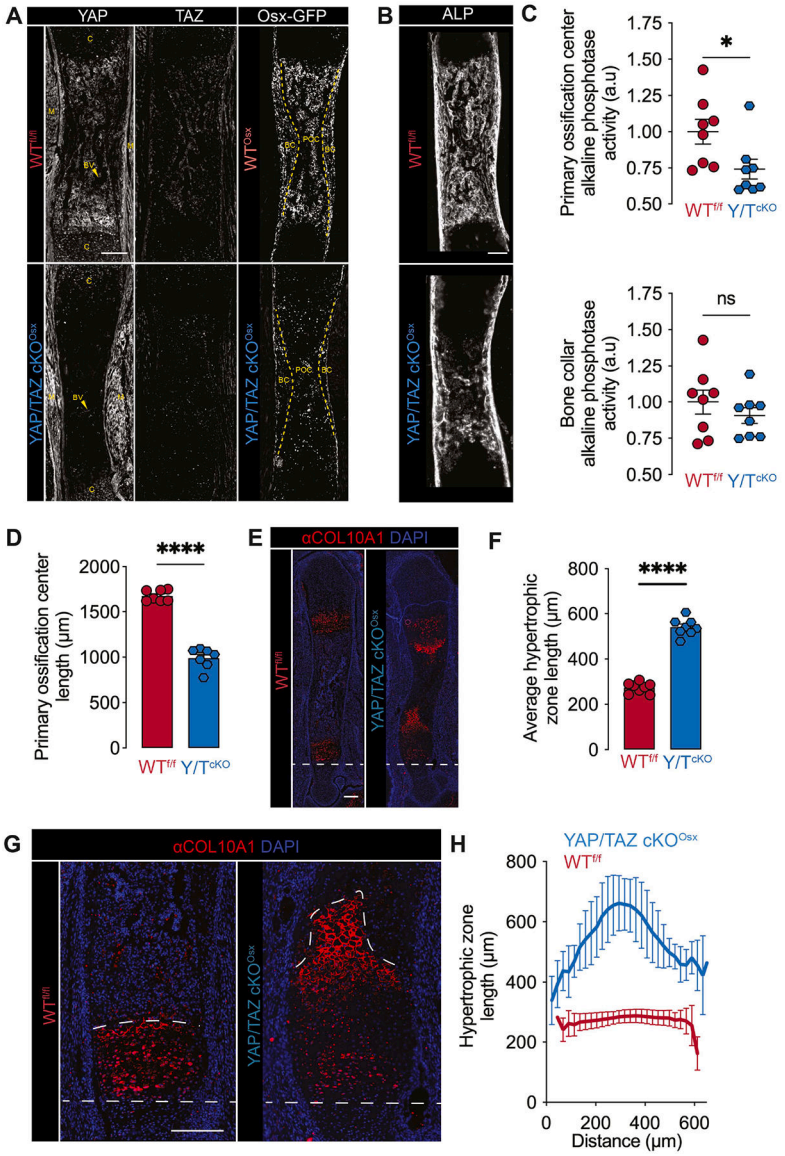

Figure 1. YAP/TAZ mediate endochondral ossification in fetal development.

(**A**) YAP, TAZ, and Osx-GFP immunostains in embryonic day 17.5 (E17.5) humeri (n= 2–4). Dotted lines mark the boundary between primary ossification center and bone collar. M – muscle; C – cartilage; POC – primary ossification center; BC – bone collar; BV – blood vessel. (**B**) Representative alkaline phosphatase (ALP) activity stain in E17.5 femurs (n=8). (**C**) Quantification of ALP activity by region of interest. (**D**) Quantification of primary ossification center length. (**E**) Collagen-10 immunostain in $WT^{f/f}$ and YAP/TAZ cKO^{Osx} E17.5 femurs (n=8). (**F**) Quantification of average growth plate length. (**G**) Magnified images of the E17.5 growth plate stained for Collagen-10. Dotted white lines indicate the initiation of the hypertrophic zone, determined by Collagen-10 staining and chondrocyte morphology. (**H**) Quantification of growth plate morphology (n = 8). Scale bars: 200 μm. Error bars: SEM, except SD in panel H. '*': $p<0.05$; '****': $p<0.0001$.

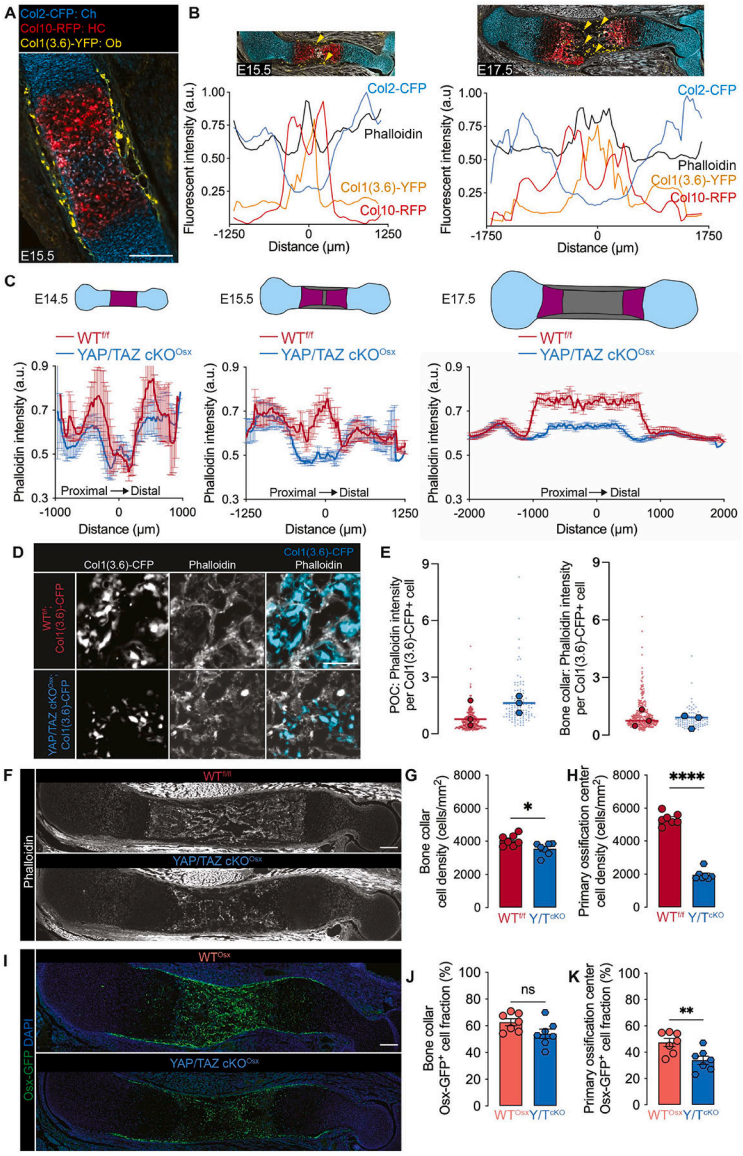

Figure 2. YAP/TAZ mediate osteoblast precursor localization and cytoskeletal dynamics in fetal bone.

(**A**) Embryonic day 15.5 (E15.5) tibia from Col2-CFP; Col10-RFP; Col1(3.6kb)-YFP transgenic reporter. (**B**) Relative fluorescent reporter and phalloidin intensity along primary axis of triple reporter humeri at E15.5 and E17.5 (n=3). Images scaled with x-axis. Phalloidin is in white. Yellow arrows indicate YFP^+ cells. (**C**) Quantification of Phalloidin intensity along the longitudinal humeral axis of $WT^{f/f}$ and YAP/TAZ cKO^{Osx} limbs (E14.5: n =3–4, E15.5: n=6, E17.5: n=7). Error bars: SEM. (**D**) Representative images of phalloidin and DAPI in the primary ossification center of E17.5 humeri from $WT^{f/f}$;Col1(3.6)-CFP and YAP/TAZ cKO^{Osx};Col1(3.6)-CFP mice. (**E**) Quantification of Phalloidin intensity in CFP^+ cells in $WT^{f/f}$;Col1(3.6)-CFP and YAP/TAZ cKO^{Osx};Col1(3.6)-CFP humeri. Large symbols indicate averages for each mouse. Small symbols indicate single cell measurements (n = 84–302 cells in N = 3 mice). (**F**) Representative phalloidin image in E17.5 humeri. (**G,H**) Quantification of cells per area by DAPI in E17.5 femurs. (**I**) Representative image

of Osx-GFP and DAPI in E17.5 humeri. (**J,K**) Fraction of Osx-GFP-expressing cells in 17.5 femurs. Scale bar: 200 μm in A, F, I. Scale bar: 100 μm in D. Error bars: SEM. '*': $p<0.05$; '**': $p<0.01$; '****': $p<0.0001$.

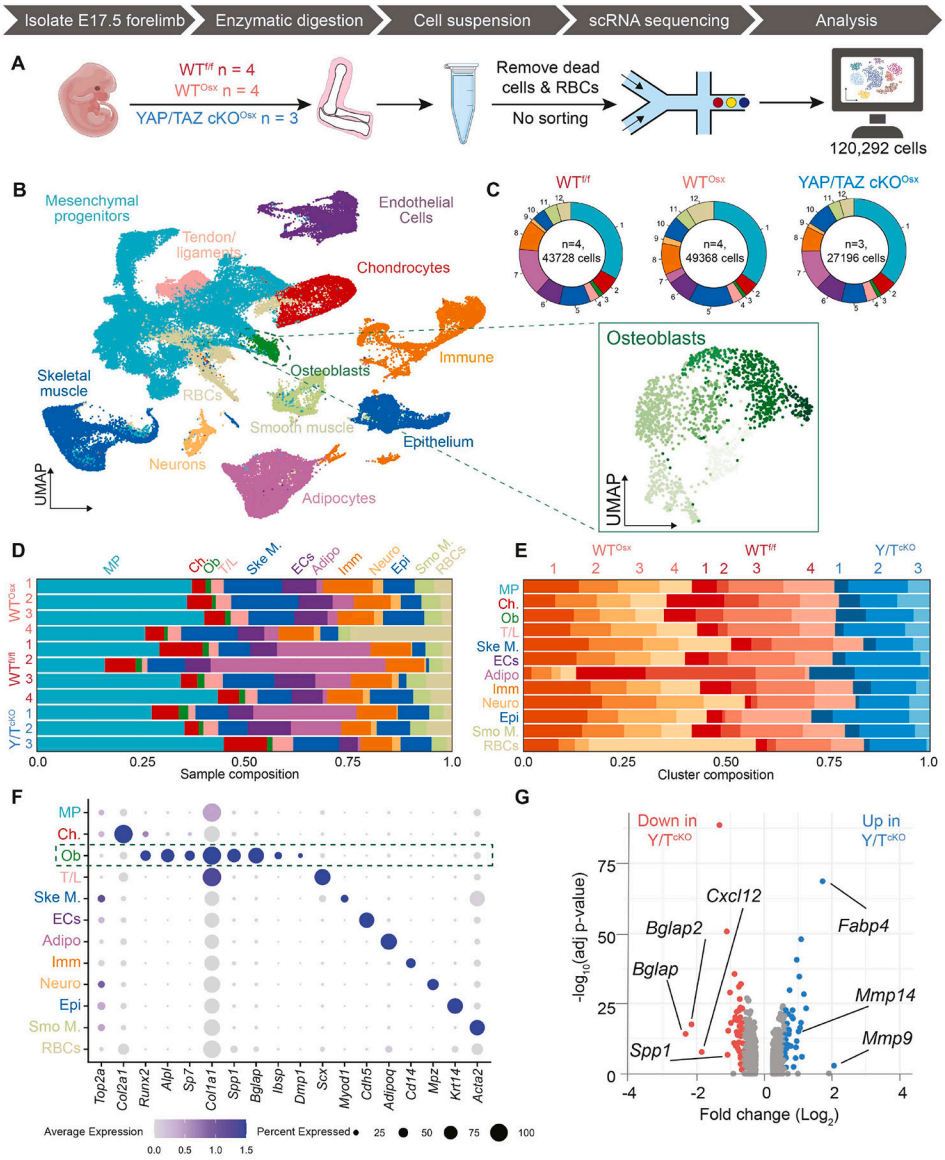

Figure 3. Identification of osteoblasts in embryonic day 17.5 fetal forelimbs by single-cell RNA sequencing.

(A) Schematic of single-cell RNA sequencing (scRNA-seq) experiment design. Fetal forelimbs, without autopod, from wildtype floxed ($WT^{f/f}$), wildtype Osx-GFP::Cre (WT^{Osx}), and Osx-conditional YAP/TAZ knockout (YAP/TAZ cKO^{Osx}) were digested at E17.5 for scRNA-seq (n = 3–4 per genotype). **(B)** Uniform manifold approximation and projection (UMAP) of integrated scRNA-seq data, labelled by corresponding cell type and iterative UMAP representation of scRNA-seq data of osteoblasts. (**C**) Proportion of cell populations within genotypes. The sample size and cell number for each genotype is indicated inside the doughnut plot (**D**). Bar plot showing the composition of each independent embryo sample by cell populations. (**E**) Bar plot showing the composition of each major cell population by sample. (**F**) Dot plot showing expression of key markers. The green box highlights osteoblasts. (**G**) Volcano plot showing differentially expressed genes between WT^{Osx} and YAP/TAZ cKO^{Osx} osteoblasts.

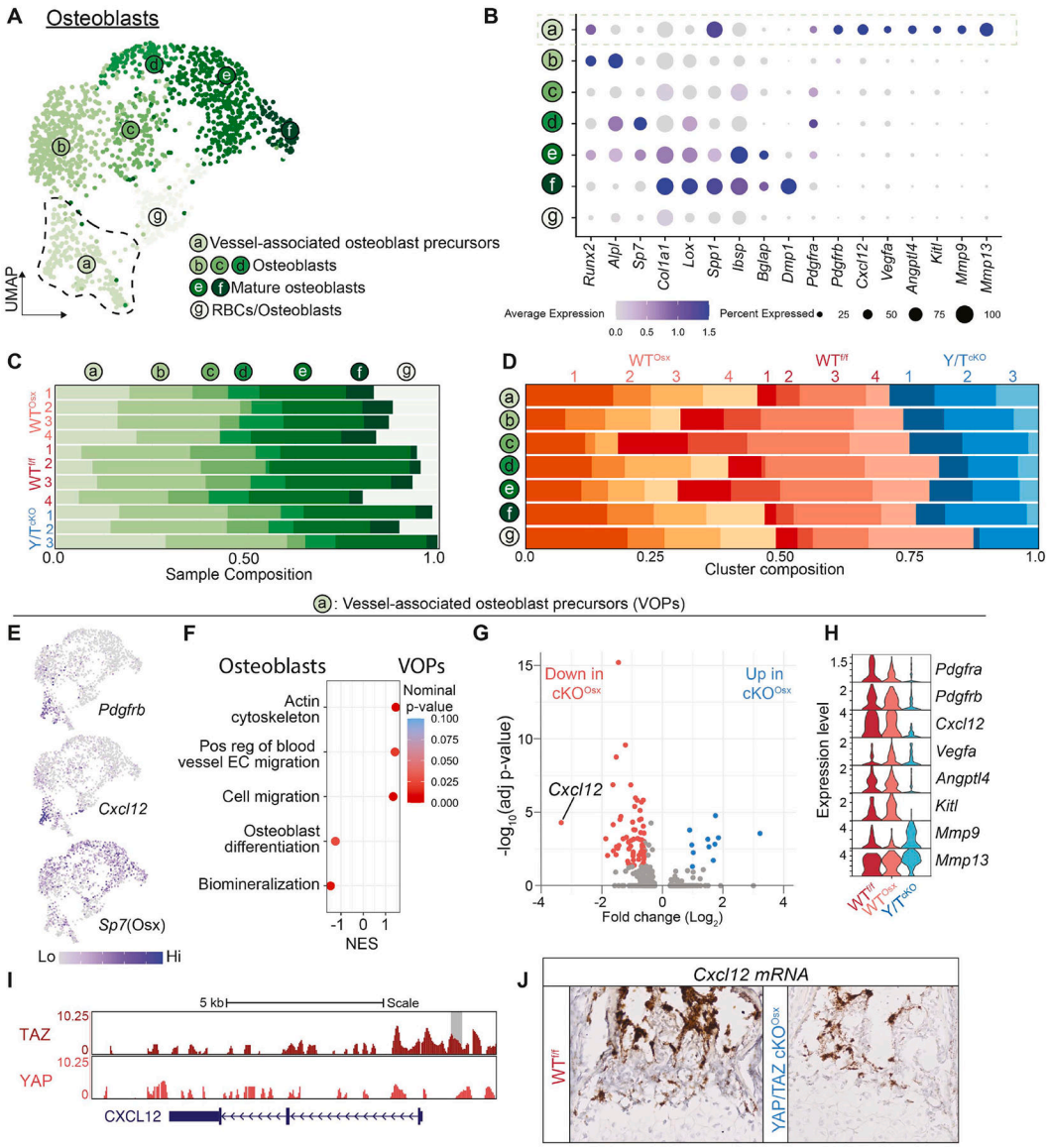

Figure 4. YAP/TAZ regulate Cxcl12 in vessel-associated osteoblast precursors (VOPs).

(A) UMAP of iterative osteoblast-lineage clusters indicating six osteoblast lineage cell states (a-f) and one characterized by erythrocyte co-lysis (g). (**B**) Dot plot showing expression of osteoblast markers. Green box highlights unique expression profile in cluster (a). **(C)** Bar plot showing the composition of each independent embryo sample's osteoblast cell states. (**D**) Bar plot showing the composition of each osteoblast cell state by sample. **(E)** Gene set enrichment analysis comparing VOPs against the other osteoblast cell states. NES, Normalized Enrichment Score. A positive NES indicates VOPs are enriched compared to the other osteoblast clusters in composite. A negative NES indicates the other osteoblasts clusters, in composite, are enriched compared to VOPs. **(F)** Gene plot showing *Pdgfrb*, *Cxcl12,* and *Sp7* (Osx) expression in osteoblast-lineage cells. **(G)** Volcano plot showing differential gene expression in VOPs. **(H)** Gene expression of select VOP-specific genes split by genotype. (**I**) ChIPseq enrichment tracks for input subtracted WT TAZ (n=1) and

YAP (n=1) binding at the CXCL12 locus. Gray bar indicates significant binding peak of TAZ slightly upstream of the CXCL12 promoter (p = 1.25e-8). Tracks visualized through http://genome.ucsc.edu. **(J)** RNAscope *in situ* hybridization of *Cxcl12* mRNA in E17.5 growth plates (n = 1–2). Scale bar: 200 μm.

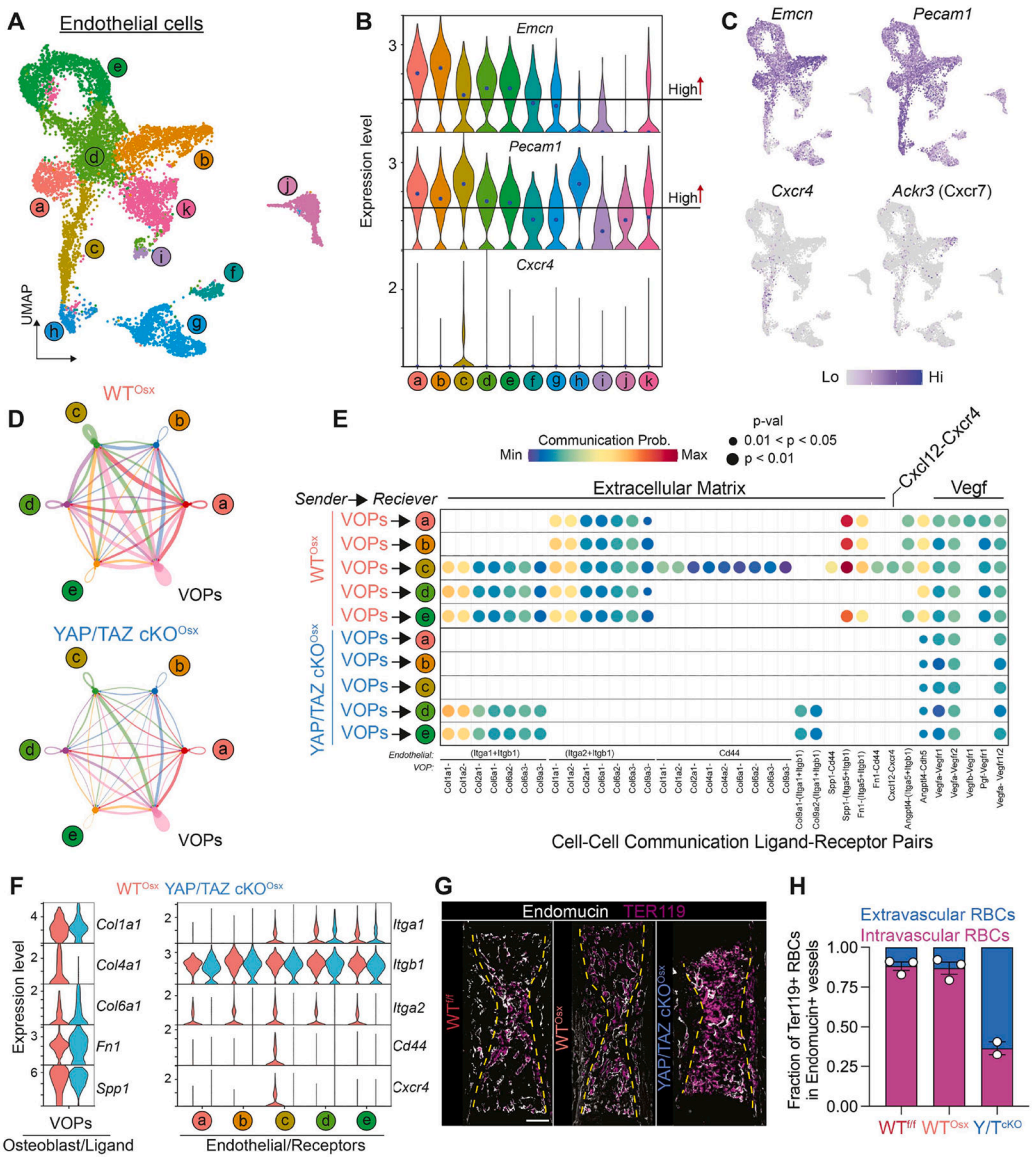

Figure 5. YAP/TAZ mediate vessel-associated osteoblast precursor (VOP)-endothelial cell crosstalk and vessel barrier function of primary ossification center blood vessels.

(**A**) UMAP of iterative endothelial cell clusters, indicating 11 endothelial cell states. (**B**) Gene expression analysis of Endomucin (*Emcn*), CD31 (*Pecam1*), and *Cxcr4*. (**C**) Gene plot showing *Emcn*, *Pecam1, Cxcr4*, and *Ackr3* (Cxcr7) expression in endothelial cells. (**D**) Circle plot showing the number of significant interactions between cell states for WT^{Osx} and YAP/TAZ cKO^{Osx}. Thickness of the line indicates the number of interactions. Color of the line indicates the source of the ligand for each ligand-receptor interaction. (**E**) Bubble plot showing significant ligand-receptor pairs between VOPs and endothelial cell states (a-e) for COLLAGEN, SPP1, FN1, CXCL, ANGPTL, and VEGF pathway signaling. The color of the dot represents the communication probability, while the presence and size indicate the p-value. (**F**) Violin plot showing the expression of VOP 'ligands' and endothelial 'receptors' from (E) in clusters (a-e). **(G)** Immunofluorescent staining of erythrocyte-marker, Ter119, and Endomucin, in $WT^{f/f}$, WT^{osx}, and YAP/TAZ cKO^{osx} E17.5 forelimbs, to

indicate extravascular erythrocytes. **(H)** Quantification of the fraction of intravascular vs. extravascular erythrocytes. Scale bars: 200 μm. RBC: Red blood cells.

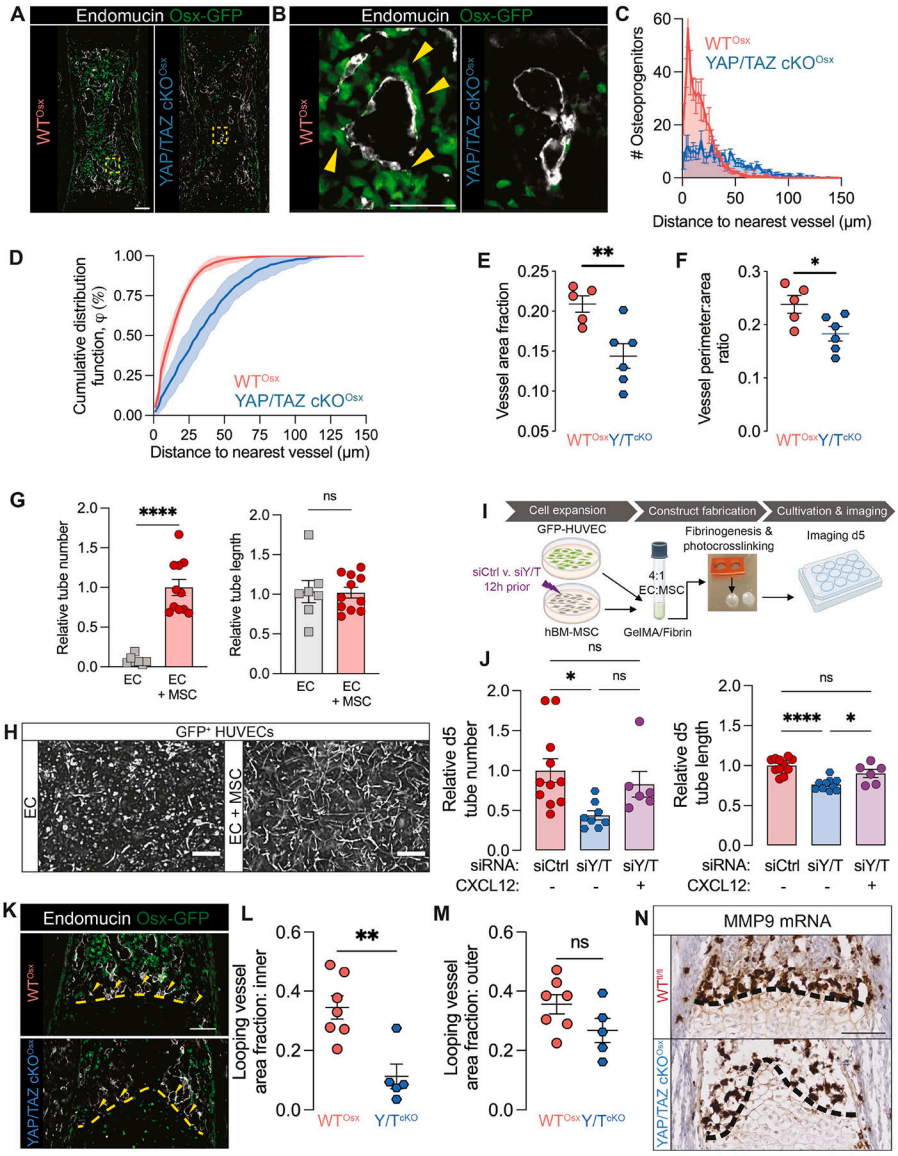

Figure 6. YAP/TAZ-Cxcl12 signaling spatially couples vessel-associated osteoblast precursors (VOPs) to angiogenesis in fetal bone.

(**A**) Representative images of Endomucin immunostains in E17.5 humeri (n=5–6). (**B**) Magnified image of (A). Scale bar: 50 μm. Yellow arrows indicate blood vessel-adjacent Osx-GFP$^+$ cells. (**C**) Histogram of the distance from each Osx-GFP$^+$ cell to the nearest Endomucin$^+$ vessel. (**D**) Cumulative distribution function of the distance from each Osx-GFP$^+$ cell to the nearest Endomucin$^+$ vessel. Error bars are SD. (**E**) Quantification of Endomucin-labelled blood vessel area relative to total area in the primary ossification center. (**F**)Measurement of average vessel size, quantified by cross-sectional perimeter to area ratio. (**G**) Quantification of relative tube number and tube length in GFP$^+$ HUVEC 3D co-culture with and without hMSCs. (**H**) Representative images of HUVEC tube morphology after 5 days. Scale bar: 500 μm. (**I**) Schematic of 3D co-culture HUVEC + hMSC experiment with siRNA-mediated YAP/TAZ depletion from hMSCs and exogenous recombinant CXCL12 (100 ng/ml) rescue. (**J**) Quantification of relative tube number and tube length at day 5

following YAP/TAZ depletion in hMSCs and CXCL12 rescue. siCtrl: non-targeting control. siY/T: siRNA depletion of YAP and TAZ. (**K**) Representative images of anastomotic looping vessels in E17.5 humeri. Yellow line indicates the chondro-osseous junction. Yellow arrows indicate Endomucin^{+} looping vessels adjacent to the chondro-osseous junction. (**L,M**) Quantification of looping vessels in the core and annulus regions adjacent to the growth plate. (**N**) RNA scope of *Mmp9* mRNA at the chondro-osseous junction (n=2). Scale bars: 100 μm, unless stated otherwise. Error bars: SEM unless stated otherwise. '*': $p<0.05$; '**': $p<0.01$; '****': $p<0.0001$.

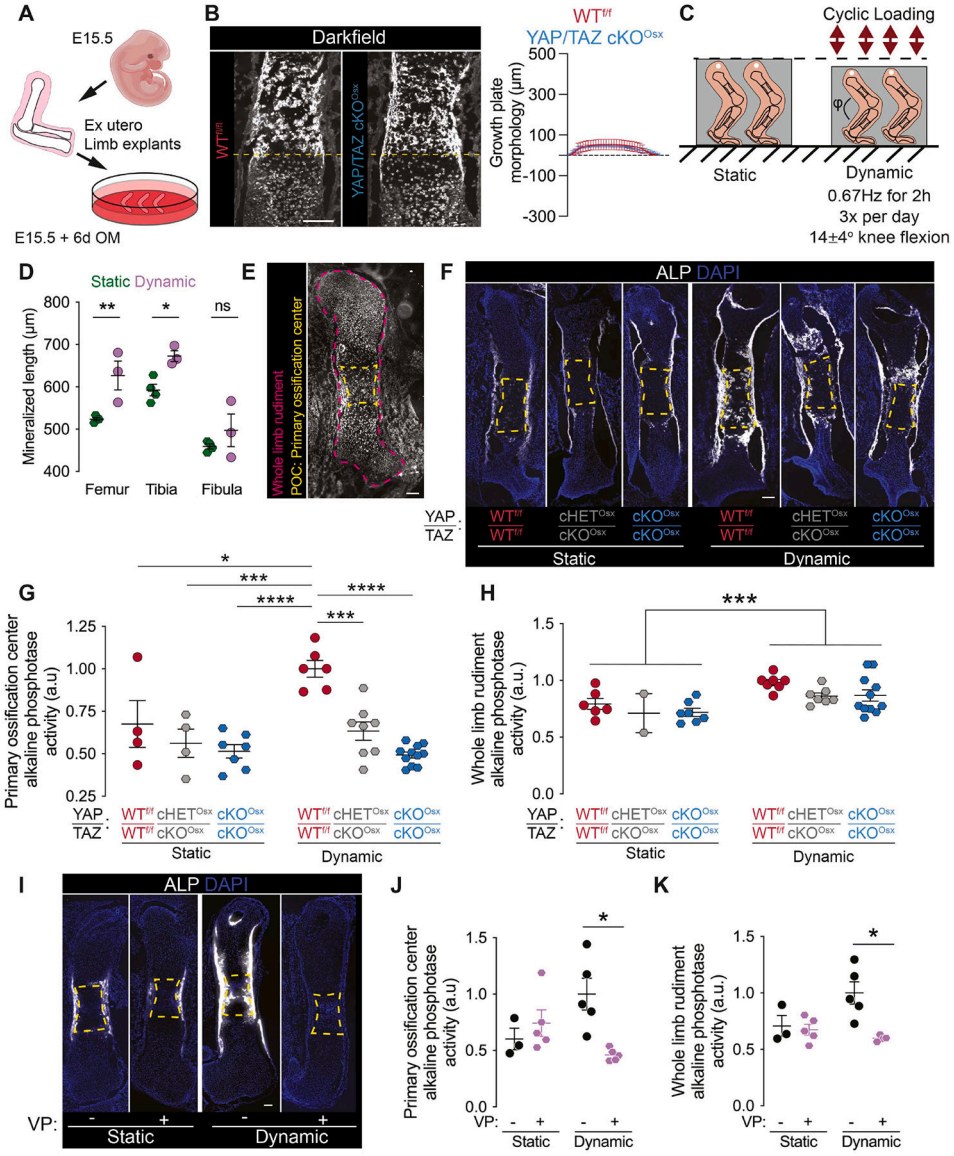

Figure 7. YAP/TAZ mediate mechanoregulation of fetal bone formation *ex vivo*.

(**A**) Schematic of explant culture. (**B**) Growth plate morphogenesis in E15.5 explanted hindlimbs after 6 days static culture and quantification of growth plate morphology. Yellow lines indicate the start of the growth plate morphology measurement. (**C**) Schematic of bioreactor-based mechanical loading of explanted fetal hindlimbs. (**D**) Quantification of mineralized rudiment length in C57Bl6 in static and dynamic conditions after 5 days culture by optical projection tomography. (**E**) Regions of interest indicating whole rudiment (magenta) and primary ossification center (yellow). (**F**) Representative images of alkaline phosphatase (ALP) activity stains. Floxed allele controls indicated by YAP $WT^{f/f}$/TAZ $WT^{f/f}$ are $WT^{f/f}$ mice. YAP heterozygous, TAZ homozygous knockout mice indicated by YAP $cHET^{Osx}$/TAZ cKO^{Osx}. Homozygous YAP/TAZ knockout mice indicated by YAP cKO^{Osx}/TAZ cKO^{Osx}. (**G, H**) Quantification of ALP activity stain. Differences determined by 2-way ANOVA with post hoc Sidek's multiple comparisons. (**L**) Representative images of ALP

activity stains. (**J,K**) Quantification of ALP activity stain. Scale bars: 100 μm. Error bars: SEM. Only significantly different comparisons are indicated. Groups without significant differences (i.e. adjusted p-value > 0.05) are not shown. p-values were determined by 2-way ANOVA with post hoc Sidek's multiple comparisons. '*': $p<0.05$; '**': $p<0.01$; '***': $p<0.001$; '****': $p<0.0001$.

KEY RESOURCES TABLE

REAGENT or RESOURCE	SOURCE	IDENTIFIER
Antibodies		
Rabbit monoclonal anti-YAP	Cell Signaling Technology	Cat#: 14074
Rabbit polyclonal anti-TAZ	Invitrogen	Cat#: PA1-46190
Rabbit polyclonal anti-Collagen10	Abcam	Cat#: ab182563
Chicken polyclonal anti-GFP	Abcam	Cat#: Ab13970
Rat monoclonal anti-Endomucin	Santa cruz	Cat#: sc-65495
APC monoclonal anti-mouse Ter119	BioLegend	Cat#: 116211
Alexa-fluor conjugated Phalloidin	Invitrogen	Cat#: A22287
Chemicals, peptides, and recombinant proteins		
CXCL12/SDF-1	R&D Systems	Cat#: 350-NS
Verteporfin	Selleck Chemicals	Cat#: S1786
Critical commercial assays		
Vector blue Alkaline phosphatase substrate kit	Vector	Cat#: SK-5300
Red Blood Cell Lysis kit	Miltenyi Biotec	Cat#: 130-094-183
Dead Cell Removal kit	Miltenyi Biotec	Cat#: 130-090-101
Deposited data		
Raw and analyzed data	This paper	GEO: GSE227818
ChIP seq data	Ong, et al[18]	GEO: GSE163458
Experimental models: Cell lines		
HUVECs	Angio-Proteomie	Cat#: cAP-0001GFP
hMSCs: RoosterVial-hBM-1M	RoosterBio	Cat#: MSC-003
Experimental models: Organisms/strains		
Mouse: YAP/TAZ cKO^{Osx}: YAP$^{fl/fl}$;TAZ$^{fl/fl}$;Osx1-GFP::Cre	Kegelman, et al[9]	N/A
Mouse: WT$^{f/f}$: YAP$^{fl/fl}$;TAZ$^{fl/fl}$	Kegelman, et al[9]	N/A
Mouse: WT^{Osx}: YAP$^{WT/WT}$; TAZ$^{WT/WT}$;Osx1-GFP::Cre	This paper	N/A
Mouse: WT$^{f/f}$;Col1(3.6)-CFP: YAP$^{fl/fl}$;TAZ$^{fl/fl}$; Col1(3.6kb)-CFP	This paper	N/A
Mouse: YAP/TAZ cKO^{Osx};Col1(3.6)-CFP: YAP$^{fl/fl}$;TAZ$^{fl/fl}$;Osx1-GFP::Cre; Col1(3.6kb)-CFP	This paper	N/A
Mouse: Triple reporter	Dyment, et al[60]	N/A
Mouse: C57/Bl6	The Jackson Laboratory	RRID:IMSR_JAX:000664
Recombinant DNA		
Stealth RNAi™ siRNA Yap1	Thermo Fisher Scientific	Cat#: 1299001
Stealth RNAi™ siRNA WWTR1/TAZ	Thermo Fisher Scientific	Cat#: 1299001
Stealth RNAi™ siRNA Negative Control Kit	Thermo Fisher Scientific	Cat#: 12935100
Software and algorithms		
Seurat	Hao and Hao, et al[62]	https://github.com/satijalab/seurat

REAGENT or RESOURCE	SOURCE	IDENTIFIER
CellChat	Jin, et al[21]	https://github.com/sqjin/CellChat
ScType	Ianevski, et al[64]	https://github.com/IanevskiAleksandr/sc-type
ImageJ	Schindelin, et al[61]	https://github.com/imagej/ImageJ
Cutadapt	Martin, et al[65]	https://github.com/marcelm/cutadapt
Bowtie2	Langmead, et al[66]	https://github.com/BenLangmead/bowtie2
MACS2	Zhang, et al[67]	https://hbctraining.github.io/Intro-to-ChIPseq/lessons/05_peak_calling_macs.html